Near-field Radiation in Nanoscale Gaps

by

Poetro Lebdo Sambegoro

Submitted to the Department of Mechanical Engineering in partial fulfillment of the requirements for the degree of

Master of Science in Mechanical Engineering

at the

MASSACHUSETTS INSTITUTE OF TECHNOLOGY

January 2011

[February 2011]

Author.....
Department of Mechanical Engineering
January 26, 2011

Certified by.....
.....
Gang Chen
Carl Richard Soderberg Professor of Power Engineering
Thesis Supervisor

Accepted by.....
David E. Hardt
Chairman, Department Committee on Graduate Students

Near-field Radiation in Nanoscale Gaps

by

Poetro Lebdo Sambegoro

Submitted to the Department of Mechanical Engineering
on January 26, 2011, in partial fulfillment of the
requirements for the degree of
Master of Science in Mechanical Engineering

Abstract

The theoretical calculations for near-field radiation heat transfer based on a local dielectric constant approach indicate that the heat transfer will go to infinity as the gap becomes very small. To correct this anomaly, it has been proposed that the heat transfer through very small gaps will saturate due to the influence of nonlocal effects on the dielectric constant. Previous experiments using an AFM bi-layer cantilever reported near-field radiation heat transfer between a silica sphere and a flat plate down to a 30 nm gap. The objective of this thesis is to experimentally study thermal radiative transfer at very small separation distances. Experimental results on near-field radiation heat transfer between a silica sphere and a flat glass substrate are presented for sphere-plate separation down to a few nanometers.

The experimental results deviate substantially from the theoretical predictions for separation distance of 100 nm and start to saturate at a separation distance of 30 nm. In addition to the effect of the spatial dispersion of the dielectric constant, this saturation may be influenced by the surface roughness of the microsphere and/or repulsive electrostatic forces. Surface roughness is included in the analytical analysis of the radiative heat transfer through an approximate model based on the Proximity Force Approximation.

Thesis Supervisor: Gang Chen

Title: Carl Richard Soderberg Professor of Power Engineering

Dedication

To my family.

Acknowledgements

This thesis owes its completion to the support of numerous individuals. I would like to thank Prof. Gang Chen for the opportunity to work with him and for his guidance and encouragement. I also thank Dr. Anastassios Mavrokefalos who trained me to work on experimental aspects of this thesis and acknowledge that this thesis is a collaborative work with him. I am grateful to Dr. Sheng Shen for helping me adjust into the Nanoengineering Group environment, especially when I just joined it, and for passing his acknowledge along to me. Also to Dr. Sang Eon Han who spent countless hours of discussion to explain patiently the "physical picture". I also thank Dr. Brian Burg and Jonathan Tong who proof read this thesis. Dr. Tony Feng and Dr. Shuo Chen for help on surface roughness treatment and AFM analysis. Daniel Kraemer frequently helped to solve general experimental problems. I also thank Mr. Edwars Jacobson for helping me a lot on administrative matters. I want to thank all my lab mates in the Nanoengineering Group, especially all Power Rangers in 7-006 (Kimberlee Collins, Maria Luckyanova, Daniel Kraemer, Matthew Branham, and Kenneth McEnaney). I am grateful to the Fulbright Foundation for support accorded to me via its fellowship program. Finally, I want to thank Prof. Filino Harahap for everything he has done for me.

Table of Contents

List of Figures

Chapter 1

Introduction

Thermal radiation originates from chaotic thermal oscillations of charges inside media. Thermal oscillations of electrons in metals or ions in crystals give rise to fluctuating current densities which in turn generate electromagnetic waves, then referred to as thermal radiation. There are two types of thermally excited electromagnetic waves, propagating waves and non–propagating, or evanescent waves. Propagating waves propagate freely into free space from the surface of a medium. Evanescent waves are bound to the surface of the medium and their field decays exponentially from the surface.

1.1 Background on Near-Field Thermal Radiation

The terms near- and far field relate the distance between objects with respect to the wavelength of the corresponding electromagnetic waves. In thermal radiation the characteristic wavelength corresponds to the dominant emission wavelength given by Wien's displacement law [1]. Far field refers to the condition when the characteristic wavelength is much smaller than the characteristic length scale. In this regime electromagnetic waves can be treated without considering their phase information. Evanescent waves are neglected because their field exponentially decays. Near-field effects are considered only when the distance between objects is comparable or smaller than the characteristic wavelength. In this regime electromagnetic waves can constructively or destructively interfere with each other and evanescent waves must be taken into account since their field is not negligible near the interface.

While radiative transfer in the far field can be analyzed using Kirchoff's law, Stefan-Boltzmann's law, and Planck's law, these laws are not valid in the near-field regime. Planck himself acknowledged this shortcoming of his law when he noted in his treatment of thermal radiation that "Throughout the following ... the linear dimensions of all parts of space considered, as well as radii of curvature of all surfaces ... are large compared with the wavelengths of the rays considered" [2]. To analyze the thermal radiative heat transfer in the near-field regime, we must solve Maxwell's equations by taking thermally induced random oscillations of charges as the source of the electromagnetic waves into account. Rytov [3] pioneered this approach by proposing fluctuational electrodynamics to model thermal emission.

The fact that energy transfer is enhanced through the existence of evanescent waves when the distance between objects is relatively small compared to the characteristic wavelength has drawn interest in the field of near-field thermal radiation. Cravalho *et al.* [5] were the first to point out that the separation distance between bodies influences the radiative energy transfer through the joint contribution of interference and evanescent waves. However, they only considered the influence of evanescent waves resulting from total internal reflection, whereas additional evanescent waves with larger parallel wavevectors bound to the surface also contribute to heat transfer. Polder and van Hove [6] followed a similar approach to Rytov *et al.* [3] by using fluctuational electrodynamics to analyze heat transfer enhancement between two parallel metallic plates. This work was followed up by Loomis and Maris [7] who worked on the same problem by focusing on the evanescent wave contribution to heat transfer. Then Shchegrov *et al.* [8] pointed out the contribution of surface waves to heat transfer. Since this time many theoretical works have been carried out on near-field thermal radiation. Most of these works are performed on one-dimensional problems. They include two semi-infinite parallel plates [6, 7, 8], two semi-infinite parallel plates with coatings [9, 10], and two semi-infinite films [11]. Other geometries include a nanoparticle-point like dipole with a semi infinite plate [12] and two spheres [13]. In terms of the materials, besides numerous studies done on dielectrics [5, 49] and metals [6], some studies have also been carried out on semiconductors [14, 15, 16] and metamaterials [17, 18]. Concerning applications, thermophotovoltaics [19, 20], nanofabrication [21, 22], and imaging [23] are being looked at.

Despite the numerous theoretical studies on the effects of near-field radiation, there are only few experimental works since the early publications by Domoto *et al.* [24] and Hargreaves [25]. These include reports by Xu *et al.* [26], Kittel *et al.* [27], Narayanaswamy *et al.* [28], and Hu *et al.* [29]. The latest research by Sheng *et al.* [30], subsequently followed up by Rosseau *et al.* [31], has eventually succeeded to prove experimentally a heat transfer enhancement of three orders of magnitude compared to black body radiation. A more detailed review on the mentioned experimental research will be given in chapter 3.

The ability to enhance radiative energy transfer by evanescent waves had raised the question of the radiative energy transfer limit. Pendry [32] proposed a maximum heat transfer limit to a single mode. The results are linked to quantum information theory which dictates that the maximum heat tunneling current in any single mode is determined by the temperature alone. Materials with finite conductivity are proposed to maximize the near-field radiative transfer. On the contrary, it has been calculated that conductors do not result in significant enhancement in near-field radiative transfer [7,8]. Basu *et al.* [33] investigated the maximum achievable radiative heat flux between two parallel plates by assuming a frequency independent dielectric function with all frequencies supporting surface waves and introducing a cutoff value on the parallel wavevector component. This cutoff value corresponds to the lattice constant of the crystal. Wang *et al.* [34] studied the influence of all parameters in the Drude and the Lorentz models to maximize the near-field radiative heat flux. Ben-Abdallah *et al.* [35] finally investigated the limit of energy transfer between two arbitrarily flat media separated by a vacuum gap. An upper limit for the energy flux is derived by using a general variational approach.

Since this calculation is based on the concept of a local dielectric constant, the obtained radiative heat transfer diverges as the separation distance goes to zero. This divergence has been criticized by Pan [36]. To solve the problem, one needs to include a spatial dispersion of the dielectric constant in the calculation. Volokitin and Persson [37, 38] were the first to include the spatial dependence of the dielectric constant in the radiative heat transfer calculation. By including the spatial dispersion of the dielectric constant Chapuis *et al.* [39] and Joulain *et al.* [40] showed that the radiative heat transfer will eventually saturate when the separation distance goes to zero.

Kittel *et al.* [27] experimentally demonstrated the saturation of radiative heat transfer when the separation gap between the tip of a thermal profiler and a gold (or gallium nitride) surface was smaller than tens of nanometers. The authors proposed that this saturation originates from spatial dispersion of dielectric constant. Later on Chapuis *et al.* [39] argued that the saturation observed by Kittel *et al.* [27] was not because of non-local effects in dielectric constant but proposed that the saturation of the heat transfer is due to the saturation from the TE mode contributions which are dominant even when the separation distance is as small as 1 nm. To conclude, there is no conclusive experimental evidence so far that the spatial dispersion of the dielectric constant is responsible for the saturation of the radiative heat transfer when the separation gap becomes very small.

1.2 Objectives

The objective of this thesis is to experimentally study thermal radiative transfer at very small separation distances. To do this, we measure the near-field radiative heat transfer between a silica microsphere with a 100 μm diameter and a flat glass substrate at separation gaps down to a few nanometers.

1.3 Organization of This Thesis

Chapter 2 introduces the theoretical background on near-field thermal radiation. Chapter 3 presents the experimental setup used for this work and illustrates the refinements that were made to be able to measure radiative heat transfer at very small separations. Chapter 4 shows preliminary experimental results and our attempts to include surface roughness into the model. Finally, Chapter 5 summarizes the findings and discusses future work.

Chapter 2

Theoretical Background

This chapter provides the theoretical foundation to calculate and analyze thermal radiative heat transfer between two parallel plates. The radiative heat transfer at very small separation gaps with respect to the spatial dispersion of the dielectric constant is explained.

2.1 Near-Field Radiative Heat Transfer between Two Parallel Plates

This section introduces the theoretical foundation to calculate and analyze thermal radiative heat transfer between two parallel plates based on fluctuational electrodynamics [3, 4]. Fluctuational electrodynamics is based on the macroscopic idea that thermal radiation originates from random thermal fluctuations of volume charge densities, not from the sum of the individual charges. These fluctuations generate electromagnetic waves which then carry the energy. Theoretical derivations to calculate thermal radiation can be divided into two parts. First, the fluctuation-dissipation theorem is used to relate the fluctuating current densities to the local temperature of the emitting media. Second, Maxwell's equations are solved to calculate the electromagnetic waves resulting from the fluctuation current densities.

Consider two parallel plates separated by a vacuum gap with a distance d, as shown in Fig. 2.1. We assume that each plate (1) is semi-infinite, (2) has infinite optical thickness, (3) is at thermal equilibrium, (4) is non magnetic and isotropic, and (5) is perfectly smooth and that the plates are parallel to each other. Radiative energy transfer is calculated by computing the Poynting vector, which is the cross product of electric and

magnetic field. Maxwell's equations need to be solved first to obtain the electric and magnetic fields resulting from the fluctuation current densities.

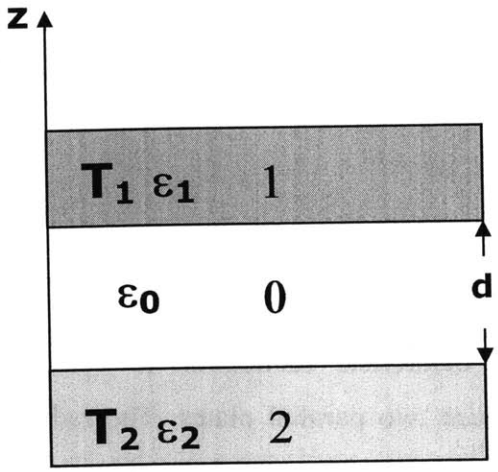

Figure 2.1 Two parallel plates at different temperatures and different optical properties separated by a vacuum gap with distance d.

2.1.1 Maxwell's Equations

Maxwell's equations are used to calculate the electromagnetic waves due to fluctuation current densities.

$$\begin{aligned} \nabla \times \boldsymbol{E} + \frac{\partial \boldsymbol{B}}{\partial t} &= 0 \\ \nabla \times \boldsymbol{H} - \frac{\partial \boldsymbol{D}}{\partial t} &= \boldsymbol{J} \\ \nabla \cdot \boldsymbol{D} &= \rho \\ \nabla \cdot \boldsymbol{B} &= 0 \end{aligned} \tag{2.1}$$

$\boldsymbol{D}$ is the displacement field, $\boldsymbol{E}$ is the electric field, $\boldsymbol{B}$ is the magnetic induction, $\boldsymbol{H}$ is the magnetic field, $\boldsymbol{J}$ is the current density and ρ is the charge density. The constitutive relation between $\boldsymbol{D}$ and $\boldsymbol{E}$, and $\boldsymbol{B}$ and $\boldsymbol{H}$ are

$$\begin{aligned} \boldsymbol{D} &= \varepsilon_0 \varepsilon \boldsymbol{E} \\ \boldsymbol{B} &= \mu_0 \mu \boldsymbol{H} \end{aligned} \tag{2.2}$$

ε_0 is the vacuum electric permittivity, ε is the relative electric permittivity, μ_0 is the vacuum magnetic permeability, and μ is the relative magnetic permeability. For time harmonic fields of the form exp(-$i\omega t$) Eq. (2.1) reduces to

$$\begin{aligned} \nabla \times \boldsymbol{E} - i\omega\mu_0\mu\boldsymbol{H} &= 0 \\ \nabla \times \boldsymbol{H} + i\omega\varepsilon_0\varepsilon\boldsymbol{E} &= \boldsymbol{J} \\ \nabla \cdot \varepsilon_0\varepsilon\boldsymbol{E} &= \rho \\ \nabla \cdot \mu_0\mu\boldsymbol{H} &= 0 \end{aligned} \tag{2.3}$$

Taking the curl of the first equation in Eq. (2.3) and substituting the curl of $\boldsymbol{H}$ from the second equation in Eq. (2.3) yields

$$\nabla \times \nabla \times \boldsymbol{E} - k^2\boldsymbol{E} = i\omega\mu_0\boldsymbol{J} \tag{2.4}$$

The response field $\boldsymbol{E}$ to the current density $\boldsymbol{J}$ can be obtained by solving Eq. (2.4). To solve Eq. (2.4) we will use the so-called Green's function method.

2.1.2 Dyadic Green's Function

The dyadic Green's function relates the vector electromagnetic field to the vector current source. The derivation in this section follows the outline by Tsang *et al.* [43]. Electric and magnetic fields are a convolution of the dyadic Green's function with the current density.

$$\boldsymbol{E}(\boldsymbol{r},\omega) = i\omega\mu_0 \int_{V'} \overline{\overline{\boldsymbol{G}}}_e(\boldsymbol{r},\boldsymbol{r}',\omega)\cdot\boldsymbol{J}(\boldsymbol{r}',\omega)\,d\boldsymbol{r}' \tag{2.5}$$

$$\boldsymbol{H}(\boldsymbol{r},\omega) = \int_{V'} \overline{\overline{\boldsymbol{G}}}_h(\boldsymbol{r},\boldsymbol{r}',\omega)\cdot\boldsymbol{J}(\boldsymbol{r}',\omega)\,d\boldsymbol{r}' \tag{2.6}$$

$$\boldsymbol{J}(\boldsymbol{r},\omega) = \int_{V'} \overline{\overline{\boldsymbol{I}}}\delta(\boldsymbol{r}-\boldsymbol{r}')\cdot\boldsymbol{J}(\boldsymbol{r}',\omega)\,d\boldsymbol{r}' \tag{2.7}$$

$\overline{\overline{\boldsymbol{G}}}_e(\boldsymbol{r},\boldsymbol{r}',\omega)$ and $\overline{\overline{\boldsymbol{G}}}_h(\boldsymbol{r},\boldsymbol{r}',\omega)$ are the dyadic green's functions for the electric and magnetic field. $\boldsymbol{r}$ and $\boldsymbol{r}'$ are the location of the response field and location of the current source, respectively. Substituting Eqs. (2.5) and (2.7) into Eq. (2.4) gives

$$\nabla \times \nabla \times \overline{\overline{\boldsymbol{G}}}_e(\boldsymbol{r},\boldsymbol{r}') - \boldsymbol{k}^2\overline{\overline{\boldsymbol{G}}}_e(\boldsymbol{r},\boldsymbol{r}') = \overline{\overline{\boldsymbol{I}}}\delta(\boldsymbol{r},\boldsymbol{r}') \tag{2.8}$$

The Dyadic Green's function is the solution for the differential equation above. Fortunately, the dyadic Green's function for one dimensional layered media is widely

known. In the case of propagation in homogeneous, isotropic infinite medium with a delta source at $\boldsymbol{r}'$, the dyadic Green's function for the electric field is given by [43]

$$\overline{\overline{\boldsymbol{G}}}_e(\boldsymbol{r},\boldsymbol{r}')=\begin{cases}\dfrac{i}{8\pi^2}\int d\boldsymbol{k}_\perp \dfrac{1}{k_z}\left[\hat{\boldsymbol{e}}(k_z)\hat{\boldsymbol{e}}(k_z)+\hat{\boldsymbol{h}}(k_z)\hat{\boldsymbol{h}}(k_z)\right]e^{i\boldsymbol{k}(\boldsymbol{r}-\boldsymbol{r}')} \\ \dfrac{i}{8\pi^2}\int d\boldsymbol{k}_\perp \dfrac{1}{k_z}\left[\hat{\boldsymbol{e}}(-k_z)\hat{\boldsymbol{e}}(-k_z)+\hat{\boldsymbol{h}}(-k_z)\hat{\boldsymbol{h}}(-k_z)\right]e^{i\boldsymbol{K}(\boldsymbol{r}-\boldsymbol{r}')}\end{cases} \tag{2.9}$$

$\hat{\boldsymbol{e}}(\pm k_z)=(k_y\hat{\boldsymbol{x}}-k_x\hat{\boldsymbol{y}})/k_\rho$ and $\hat{\boldsymbol{h}}(\pm k_z)=\mp k_z/\boldsymbol{k}(k_x\hat{\boldsymbol{x}}+k_y\hat{\boldsymbol{y}})/k_\rho+k_\rho/k\hat{\boldsymbol{z}}$ are unit vectors perpendicular to $(k_x\hat{\boldsymbol{x}}+k_y\hat{\boldsymbol{y}}\pm k_z\hat{\boldsymbol{z}})$, $\boldsymbol{k}_\perp=k_x\hat{\boldsymbol{x}}+k_y\hat{\boldsymbol{y}}$, $\boldsymbol{k}=k_x\hat{\boldsymbol{x}}+k_y\hat{\boldsymbol{y}}+k_z\hat{\boldsymbol{z}}$, and $\boldsymbol{K}=k_x\hat{\boldsymbol{x}}+k_y\hat{\boldsymbol{y}}-k_z\hat{\boldsymbol{z}}$. k_x and k_y are the in-plane components of the wave vector, k_z is the out-of-plane component, and $k_\rho=\sqrt{k_x^2+k_y^2}$. The Green's function in layered materials that do not contain a delta source, which we shall call the homogeneous part, is given by [43]

$$\begin{aligned}\overline{\overline{\boldsymbol{G}}}_e(\boldsymbol{r},\boldsymbol{r}')=\frac{i}{8\pi^2}\int d\boldsymbol{k}_\perp \frac{1}{k_z}\Big\{&\left[A_l\hat{\boldsymbol{e}}_l(k_{lz})e^{i\boldsymbol{k}_l\cdot\boldsymbol{r}}+B_l\hat{\boldsymbol{e}}_l(-k_{lz})e^{i\boldsymbol{K}_l\cdot\boldsymbol{r}}\right]\hat{\boldsymbol{e}}(-k_z)e^{-i\boldsymbol{K}\cdot\boldsymbol{r}'} \\ &\left[C_l\hat{\boldsymbol{h}}_l(k_{lz})e^{i\boldsymbol{k}_l\cdot\boldsymbol{r}}+D_l\hat{\boldsymbol{h}}_l(-k_{lz})e^{i\boldsymbol{K}_l\cdot\boldsymbol{r}}\right]\hat{\boldsymbol{h}}(-k_z)e^{-i\boldsymbol{K}\cdot\boldsymbol{r}'}\Big\}\end{aligned} \tag{2.10}$$

For the case of two parallel plates, Eq. (2.10), the Green's function for electric field in layer 2 due to current source in layer 1 and vice versa, can be simplified to

$$\begin{aligned}\overline{\overline{\boldsymbol{G}}}_e(\boldsymbol{r},\boldsymbol{r}')=\frac{i}{8\pi^2}\int d\boldsymbol{k}_\perp \frac{1}{k_z}\Big\{&T^{TE}\hat{\boldsymbol{e}}_t(-k_{tz})e^{i\boldsymbol{K}_t\cdot\boldsymbol{r}}\hat{\boldsymbol{e}}(-k_z)e^{-i\boldsymbol{K}\cdot\boldsymbol{r}'} \\ &+T^{TM}\hat{\boldsymbol{h}}_t(-k_{tz})e^{i\boldsymbol{K}_t\cdot\boldsymbol{r}}\hat{\boldsymbol{h}}(-k_z)e^{-i\boldsymbol{K}\cdot\boldsymbol{r}'}\Big\}\end{aligned} \tag{2.11}$$

Using Maxwell's equations it can be shown that

$$\overline{\overline{\boldsymbol{G}}}_h=\nabla\times\overline{\overline{\boldsymbol{G}}}_e \tag{2.12}$$

Now we can calculate the electric and magnetic fields in region 2 resulting from a current source in region 1 and vice versa by substituting Eq. (2.11) back into Eqs. (2.5) and (2.6). Coefficients *A*, *B*, *C*, *D* in Eq. (2.10) and the transmission coefficient T^{TE} and T^{TM} in Eq. (2.11) can be determined by satisfying boundary conditions at the interface. The transfer matrix method is generally used to calculate these coefficients [43, 45].

2.1.3 Poynting Vector

The radiative energy flux is be determined by calculating the Poynting vector.

$$\langle S(r,\omega)\rangle = \frac{1}{2}\mathrm{Re}\left(E \times H^*\right) \tag{2.13}$$

The brackets denote a statistical ensemble average. The components of the cross products can then be written as [46]

$$\left\langle E_i H_j^* \right\rangle = i\omega\mu_0 \int_{V'} dr' \int_{V'} dr'' \overline{\overline{G}}_{e_{ik}}(r,r',\omega)\overline{\overline{G}}_{h_{jl}}(r,r',\omega)\left\langle J_k(r')J_l(r'')\right\rangle \tag{2.14}$$

Notice that for two parallel plates we are only interested in the Poynting vector in the z-direction.

2.1.4 Fluctuation-Dissipation Theorem

In Eq. (2.14) the spectral density of the current density (i.e., the ensemble average of the spatial correlation function of the current density) is required to calculate the Poynting vector. The fluctuating current densities originate from random thermal charge fluctuations. The Fluctuation Dissipation Theorem (FDT) is used to relate the spectral density of the current density to the local temperature of a medium [44, 46, 47, 48].

$$\begin{aligned}\left\langle \boldsymbol{J}_k(\boldsymbol{r},\omega)\boldsymbol{J}_l^*(\boldsymbol{r}',\omega)\right\rangle &= \lim_{r'\to r}\frac{1}{\Delta V'}\frac{\varepsilon_0\varepsilon''(\omega)\omega\theta(\omega,T)}{\pi}\delta_{kl} \\ &= \frac{\varepsilon_0\varepsilon''(\omega)\omega\theta(\omega,T)}{\pi}\delta_{kl}\delta(r-r')\end{aligned} \tag{2.15}$$

$\theta(\omega,T)$ is the mean energy of the Planck oscillator at frequency ω and in thermal equilibrium T.

$$\theta(\omega,T) = \frac{\hbar\omega}{2} + \frac{\hbar\omega}{\exp(\hbar\omega/k_B T)-1} \tag{2.16}$$

$\hbar = h/2\pi$ is Planck's constant over 2π and k_B is the Boltzmann constant. The term $\hbar\omega/2$ accounts for the zero-point energy and is necessary in the Casimir force calculation. This term can however be omitted in the net radiative heat flux calculation, since it cancels out. Eq. (2.15) can then be substituted into Eq. (2.14) to calculate the Poynting vector. δ_{kl} assumes that the medium is isotropic. There is no coupling between

currents with orthogonal direction. $\delta(\boldsymbol{r}-\boldsymbol{r}')$ assumes that the current at point $\boldsymbol{r}'$ is decorrelated from the current at point $\boldsymbol{r}$. This is often called a local approach.

2.1.5 Results and Discussions

After a series of mathematical manipulations, the net radiative heat flux between two semi-infinite parallel plates separated by a vacuum gap d can be expressed as [49]

$$q_{1-2}^{net,prop} = \frac{1}{\pi^2}\int_{\omega=0}^{\infty}[\theta(\omega,T_1)-\theta(\omega,T_2)]d\omega \times \int_{k_r=0}^{\omega/c_0}\left[\frac{(1-|r_{01}^s|^2)(1-|r_{02}^s|^2)}{4|1-r_{01}^s r_{02}^s \exp(2ik_{z,0}d)|^2}+\frac{(1-|r_{01}^p|^2)(1-|r_{02}^p|^2)}{4|1-r_{01}^p r_{02}^p \exp(2ik_{z,0}d)|^2}\right]k_r dk_r \tag{2.16}$$

$$q_{1-2}^{net,evan} = \frac{1}{\pi^2}\int_{\omega=0}^{\infty}[\theta(\omega,T_1)-\theta(\omega,T_2)]d\omega \times \int_{k_r=\omega/c_0}^{\infty}\exp(-2\,\mathrm{Im}(k_{z,0})d)\left[\frac{\mathrm{Im}(r_{01}^s)\,\mathrm{Im}(r_{02}^s)}{|1-r_{01}^s r_{02}^s \exp(-2\,\mathrm{Im}(k_{z,0})d)|^2}+\frac{\mathrm{Im}(r_{01}^p)\,\mathrm{Im}(r_{02}^p)}{|1-r_{01}^p r_{02}^p \exp(-2\,\mathrm{Im}(k_{z,0})d)|^2}\right]k_r dk_r \tag{2.17}$$

Because of the symmetry, cylindrical coordinates can be used and the wavevector component becomes $\boldsymbol{k} = k_r\hat{\boldsymbol{r}} + k_z\hat{\boldsymbol{z}}$, where $\boldsymbol{k}_r$ is the wavevector component parallel to the interface and k_z is the wavevector component perpendicular to the interface. The wave vectors in media 1 and 2 are $\boldsymbol{k}_1 = \sqrt{\varepsilon_1}\boldsymbol{k}_0$ and $\boldsymbol{k}_2 = \sqrt{\varepsilon_2}\boldsymbol{k}_0$, where $k_0 = \omega/c_0 = 2\pi/\lambda$ is the magnitude of the wavevector in vacuum. r_{01} is the Fresnel reflection coefficient between medium 0 and medium 1. Superscripts denote s-polarization (TE), and p-polarization (TM), $r_{01}^s = (k_{z0}-k_{z1})/(k_{z0}+k_{z1})$, $r_{01}^p = (\varepsilon_1 k_{z0}-\varepsilon_0 k_{z1})/(\varepsilon_1 k_{z0}+\varepsilon_0 k_{z1})$, where $k_{z0} = \sqrt{k_0^2 - k_r^2}$, and $k_{z1} = \sqrt{k_1^2 - k_r^2}$. The boundary condition on the interface requires that the parallel wavevector k_r must always be the same. The parallel wavevector k_r must also be real since the amplitude of the wave may not change in the $\boldsymbol{r}$-direction. Propagating

waves exist in vacuum when k_{z0} is real ($k_r \leq \omega/c_0$). Evanescent waves exist in vacuum when k_{z0} is imaginary. In this case, the field decays exponentially in the z-direction. Eqs. (2.16) and (2.17) are the net total radiative heat flux for propagating ($k_r \leq \omega/c_0$) and evanescent modes ($k_r > \omega/c_0$), respectively.

Fig (2.2) shows the radiative heat flux between two parallel glass substrates as a function of separation distance. The total radiative heat transfer increases when the separation distance decreases. This is due to contributions from evanescent waves. When d is relatively large, the radiative transfer from evanescent modes is negligible, since evanescent fields decay exponentially in the z-direction as suggested by the factor $e^{-2\mathrm{Im}(k_z)d}$ in Eq. (2.17). When d is relatively small, the evanescent waves can tunnel to the other medium. The radiative transfer from evanescent modes becomes the dominating factor starting at micron separation distances. This heat transfer mode can be considered as an additional heat transfer channel [32] and consequently the radiative heat transfer can exceed blackbody radiation, predicted by the Stefan-Boltzmann law.

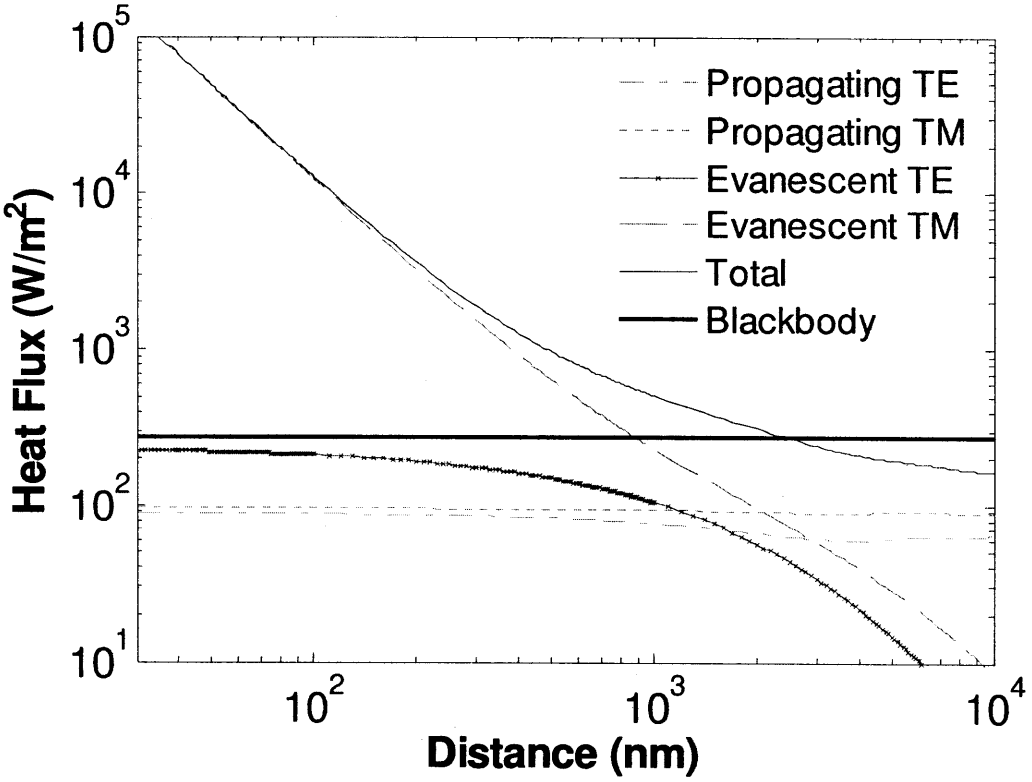

Figure 2.2 Radiative heat transfer between two parallel glass substrates as function of distance separation. $T_1 = 332.15$ K and $T_2 = 292.15$ K.

The evanescent TM modes contribute dominantly to the total radiative heat flux between two glass substrates at small separation distances. This is due to resonance modes called surface phonon polaritons. Surface polaritons are surface waves which propagate along the interface and decay exponentially on both sides of the interface [51]. Surface polaritons are polarized in the TM mode. The surface waves exist when the real part of dielectric constant is equal to -1 and the imaginary part of dielectric constant is not too large [51, 33]. There are two types of surface polaritons, surface phonon polaritons and surface plasmon polaritons. Surface plasmon polaritons originate from the coupling between the oscillations of free electrons in metals and electromagnetic waves. Surface plasmon polaritons exist in the ultraviolet (UV) and visible spectrum. Surface phonon polaritons originate from the coupling between the oscillations of optical phonons in polar dielectrics and electromagnetic waves. The phonon oscillations of charged atoms in polar materials are coupled with electromagnetic waves. Surface phonon polaritons occur in the infrared (IR) spectrum. Fig (2.3) shows the spectral radiative heat flux as a function of wavelength for two parallel glass plates separated by a 100 nm vacuum gap. Resonant peaks due to surface phonon polaritons are observed at wavelengths of 8.5 μm and 20.3 μm [50]. These two peaks correspond to specific wavelengths where the real part of dielectric constant is equal to -1, as shown in Fig (2.4). Surface phonon polaritons allow radiative heat transfer to be orders of magnitude greater than black body radiation [30, 53]. Another peak is also observed at a wavelength of 12.4 μm. This is different from the other two peaks because this peak does not originate from surface waves. This peak is due to the strong absorption of bulk polaritons as can be seen in Fig. 2.4 by a peak in the imaginary part of dielectric constant while the real part of the dielectric constant is positive.

The contribution of TE modes to the total radiative heat flux is very small. This can be seen by looking at the spectral radiative heat flux and the dielectric constant of glass. The real part of the dielectric constant is negative for certain frequency ranges where surface phonon polaritons exist in TM modes. Electromagnetic waves do not exist inside glass for these frequency ranges. While TM modes can support surface phonon polaritons at the interface between glass and vacuum, TE modes cannot. As can be seen in Fig. 2.3,

the spectral heat flux for TE modes at these frequency ranges is minimum, leading to a small contribution to the total heat transfer.

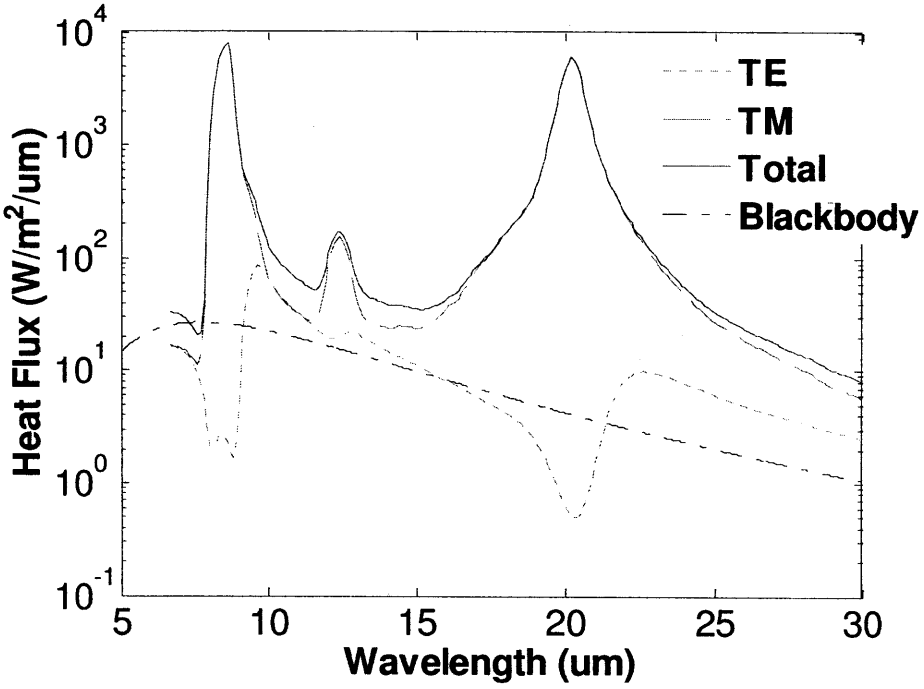

Figure 2.3 Spectral radiative heat transfer flux between two parallel glass plates separated by 100 nm vacuum gap. $T_1 = 332.15$ K and $T_2 = 292.15$ K.

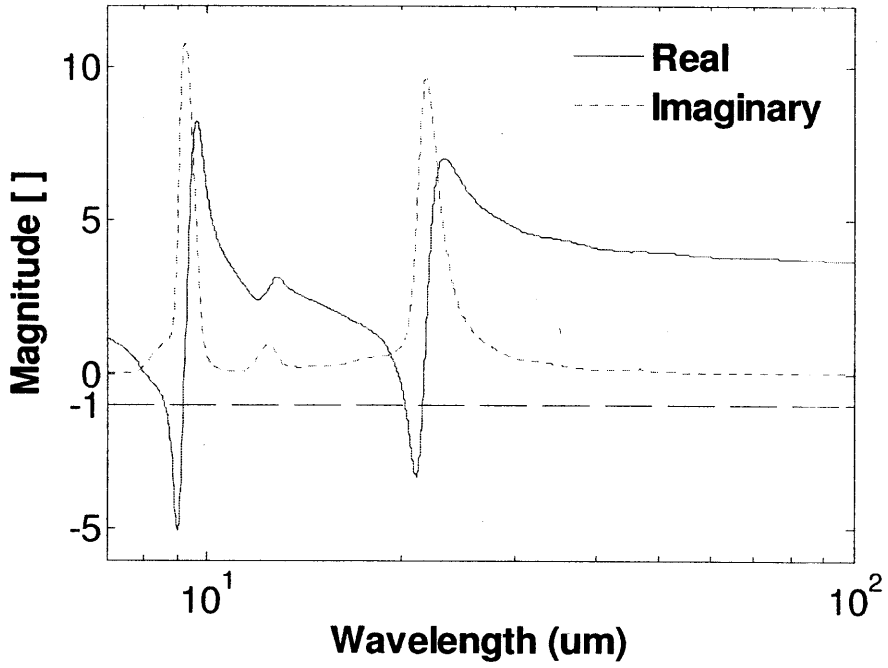

Figure 2.4 Dielectric constant of glass [54].

To understand the reason in the divergence of the heat flux of the evanescent TM modes and the saturation of the heat flux of the evanescent TE modes, Fig. 2.5 presents contour plots of the imaginary part of reflection coefficient as a function of angular frequency and parallel wavevector for both TM and TE modes. The imaginary part of the reflection coefficient is proportional to the energy density of the electromagnetic waves on the surface of the emitting medium [32]. The imaginary part of the reflection coefficient can also be considered as a generalized emissivity [49]. The area on the left side of the light line is the propagating waves region where the parallel wavevector is smaller than ω/c. The area on the right is the evanescent wave region where parallel wavevector is larger than ω/c. In Fig. 2.5a, the heat flux contribution from surface phonon polaritons can be observed at angular frequencies of ~ 2.2161×10^{14} rad/s (8.5 um) and ~ 9.2791×10^{13} (20.3 um). The heat flux due to surface phonon polaritons remains constant as parallel wavevector goes to infinity. This explains the divergence of the heat flux by surface phonon polaritons. Evanescent waves with large parallel wavevectors decay very fast. These modes do not contribute significantly to the heat transfer when the separation distance is relatively large compared to the corresponding wavelength for a particular wavevector $\lambda \sim 1/k$. As the separation distance decreases, these modes start to contribute to the heat transfer. As a consequence, the radiative heat transfer diverges when the separation distance becomes smaller since more modes with large wavevectors are able contribute to the heat transfer. The existence of TM modes with very large wavevectors is a consequence of neglecting the spatial dispersion of the dielectric constant. A brief discussion on the spatial dispersion of the dielectric constant will be given in Section 2.2.

The saturation of the heat transfer contribution due to the evanescent TE modes can be explained by Fig. 2.5b. Modes with large heat flux contribution are concentrated around the region where the parallel wave vector is not very large, i.e. $\sim 3 \times 10^6$ (rad/m). As a consequence, when the separation distance is in the order of ~100 nm every mode available already contributes to the heat transfer. Hence, there are no more modes left to be added, when the separation distance becomes smaller.

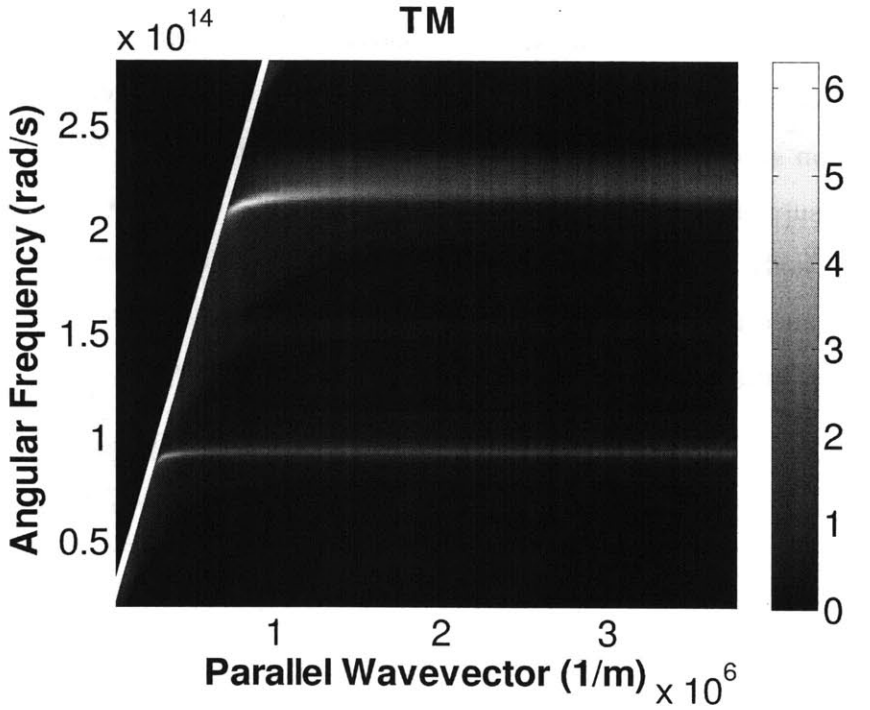

(a)

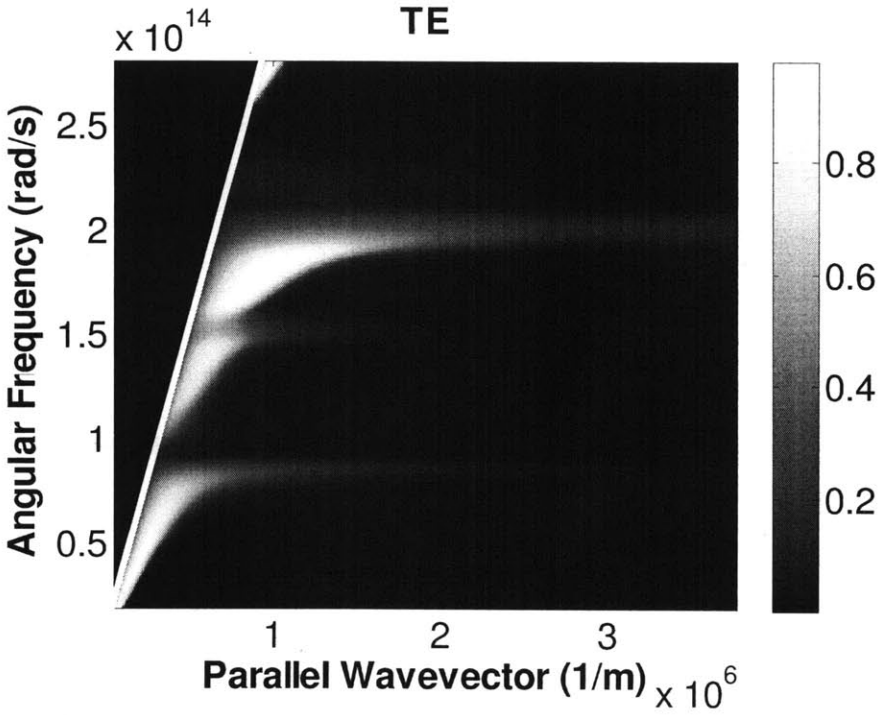

(b)

Figure 2.5 Imaginary part of reflection coefficient of (a) TM and (b) TE modes for glass. The color bar indicates the magnitude. The white diagonal line is the light line. Note that the color bar for TM modes is one order of magnitude greater than that of TE modes.

For comparison, we also calculated the radiative heat transfer between materials which do not support surface polaritons. Fig. 2.6 presents the radiative heat flux between two intrinsic silicon substrates as function of separation distance. Even though intrinsic silicon does not support surface phonon polariton, the total radiative heat flux still exceeds the black body radiation limit due to the contribution of evanescent modes. As the separation distance approaches zero, the radiative heat flux saturates at n^2 times the blackbody radiation limit [3, 35, 46], with n being the index of refraction.

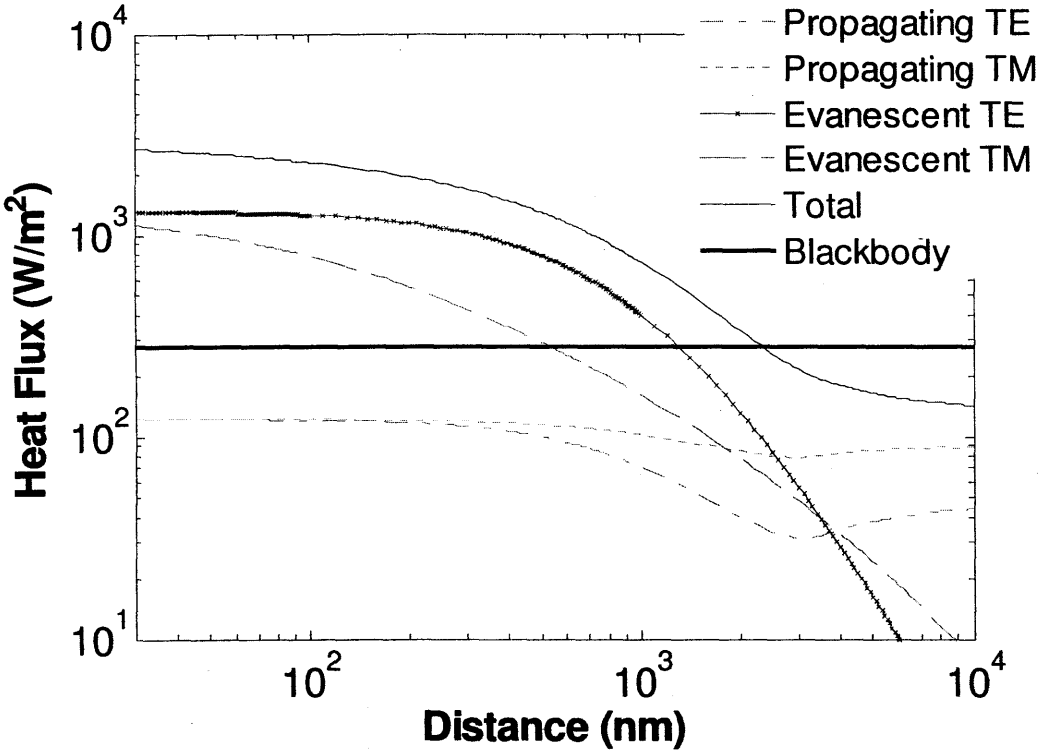

Figure 2.6 Radiative heat transfers between two parallel intrinsic silicon plates as a function of distance. $T_1 = 332.15$ K and $T_2 = 292.15$ K.

Fig. 2.7 shows the spectral radiative heat flux between two parallel intrinsic silicon plates at a separation of 100 nm. Intrinsic silicon does not support surface phonon polaritons in the infrared spectrum. The real part of the dielectric constant takes on a constant positive value in the infrared range, while the imaginary part is very small. The contribution of TE modes to the total radiative heat transfer is greater than that of TM modes.

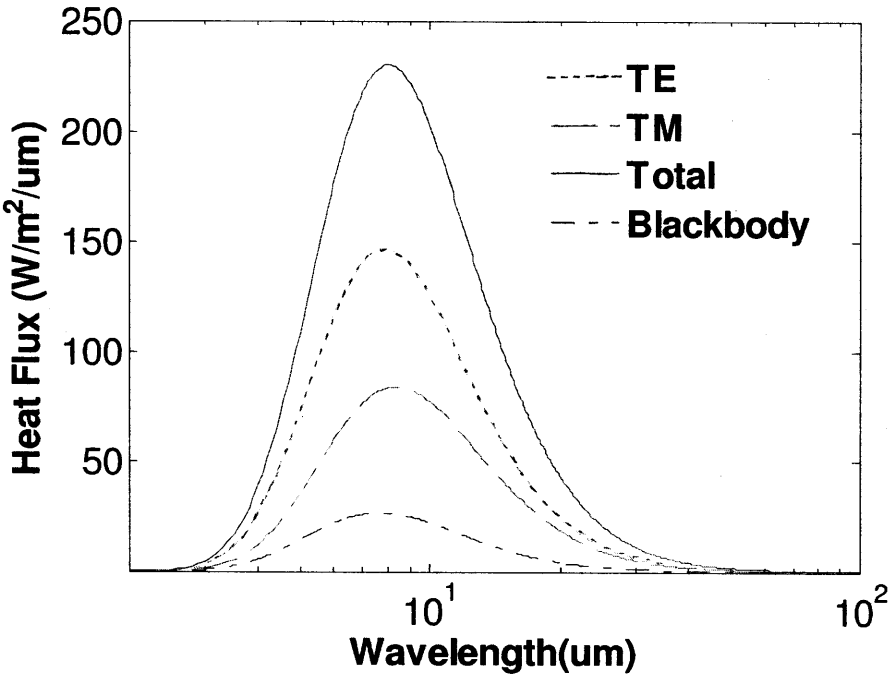

Figure 2.7 Spectral radiative heat transfer between two parallel intrinsic silicon plates separated by a 100 nm vacuum gap. $T_1 = 332$ K and $T_2 = 292$ K.

2.2 Spatial Dispersion of Dielectric Constant

As we can see from Fig. 2.5a, the divergence of the radiative heat flux at very small separation distances can be traced back to the existence of evanescent waves with very large wavevectors. These evanescent waves with very large wavevectors exist as a consequence from the local approach of the dielectric constant. By neglecting the spatial dispersion of the dielectric constant, the assumption is made that evanescent modes with very large wavevectors exist, while there actually is an upper limit for wavevectors. This upper limit of for wavevectors depends on the properties of the material.

Until this point, we assumed that the displacement field at any point $\boldsymbol{r}$ is only dependent on the electric field at the same point.

$$\boldsymbol{D}(\boldsymbol{r}) = \varepsilon(\boldsymbol{r})\boldsymbol{E}(\boldsymbol{r}) \tag{2.18}$$

In general though, the displacement field for a point $\boldsymbol{r}$ also depends on the electric field in a region of space around point $\boldsymbol{r}$ [54],

$$\boldsymbol{D}(\boldsymbol{r}) = \int \varepsilon(\boldsymbol{r}-\boldsymbol{r}')\boldsymbol{E}(\boldsymbol{r}')d^3\boldsymbol{r}' \tag{2.19}$$

This displacement field should be strongly influenced by the electric field in the vicinity of point $\boldsymbol{r}$, while the influence of the electric field further away from $\boldsymbol{r}$ will be less. Therefore we expect $\varepsilon(\boldsymbol{r}-\boldsymbol{r}',\omega)$ to be a function that decays with the distance from $\boldsymbol{r}$. The function should also depend on material properties.

The local approach assumes that $\varepsilon(\boldsymbol{r}-\boldsymbol{r}',\omega)$ is a Dirac delta function. The displacement field at point $\boldsymbol{r}$ only depends on the electric field at the same location. This implies that electromagnetic waves with any wavelength can exist and consequently to the divergence of the heat flux as shown in the previous section.

Now let's replace the delta function with a smoother function, such as a Gaussian function as depicted in Fig. 2.8 with correlation length l. In the limit where the wavelength is very large compared to the correlation length, $\boldsymbol{E(r')} \approx \boldsymbol{E(r)}$, Eq. (2.19) gives Eq. (2.18) and the local approach is valid in this limit.

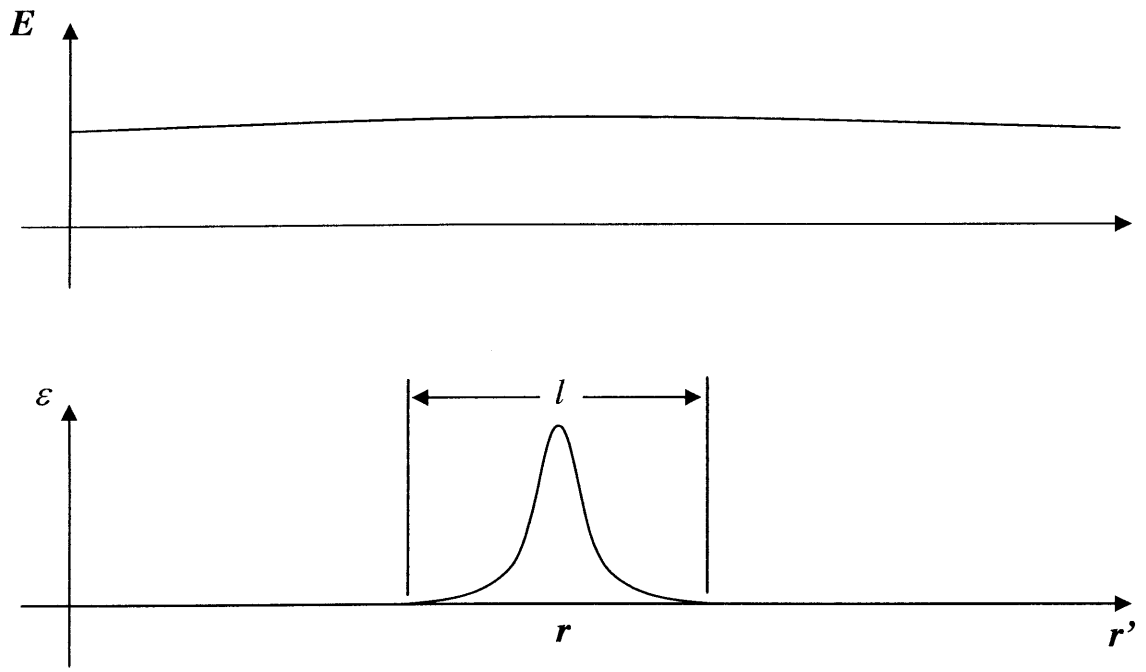

Figure 2.8 Long wavelength limit of the spatial dispersion of the dielectric constant.

We now consider Fig. 2.9 where the wavelength is comparable or shorter than the correlation length. In this case, the area in the vicinity of $\boldsymbol{r}$ does not experience the same field. The displacement field at any particular point is strongly influenced by the electric

fields in the vicinity of ***r***. When the wavelength is very short, the average value of the fields on that particular point becomes zero. In other words, that particular point does not feel the field of that particular wavelength. Thus, the correlation length sets a lower limit for the wavelength or and upper limit for the wavevector that can exist in the medium.

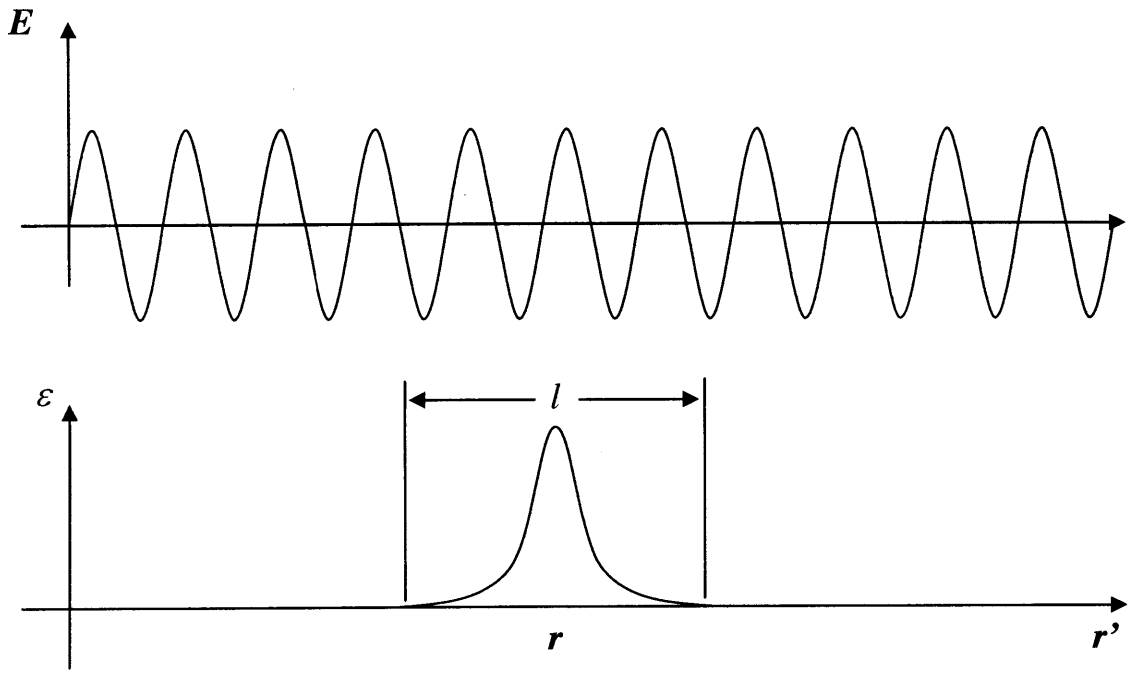

Figure 2.9 Short wavelength limit of the spatial dispersion of the dielectric constant.

For metals the correlation length is related to the Fermi length [55, 56]. For dielectrics, the lattice constant is clearly the lower limit for this length but it is not clear what actually governs the correlation length [56]. There are only few works on near-field thermal radiation which include the spatial dispersion of the dielectric constant [37, 38, 39, 42], especially on for dielectrics [40]. This is because of a lack of data on the spatial dispersion of the dielectric constant [55]. Also, since the effect of spatial dispersion on the thermal radiative heat transfer is only important at very small separation distances, the local approach has mostly led to satisfactory results. In 2005 though, Kittel *et al.* [27] published an experimental work suggesting that the effect of spatial dispersion can start to be observed at a 10 nm separation distance. This report has redrawn the attention on the influence of the spatial dispersion of dielectric constants for radiative heat transfer.

Since we do not know the spatial dispersion of the dielectric constant for glass, we cannot calculate the near-field radiative heat transfer between two glass substrates at very

small separation gaps. To illustrate the effect of the spatial dispersion of the dielectric constant on the radiative heat transfer at very small gaps, we simply impose a cut-off value on the parallel wavevector.

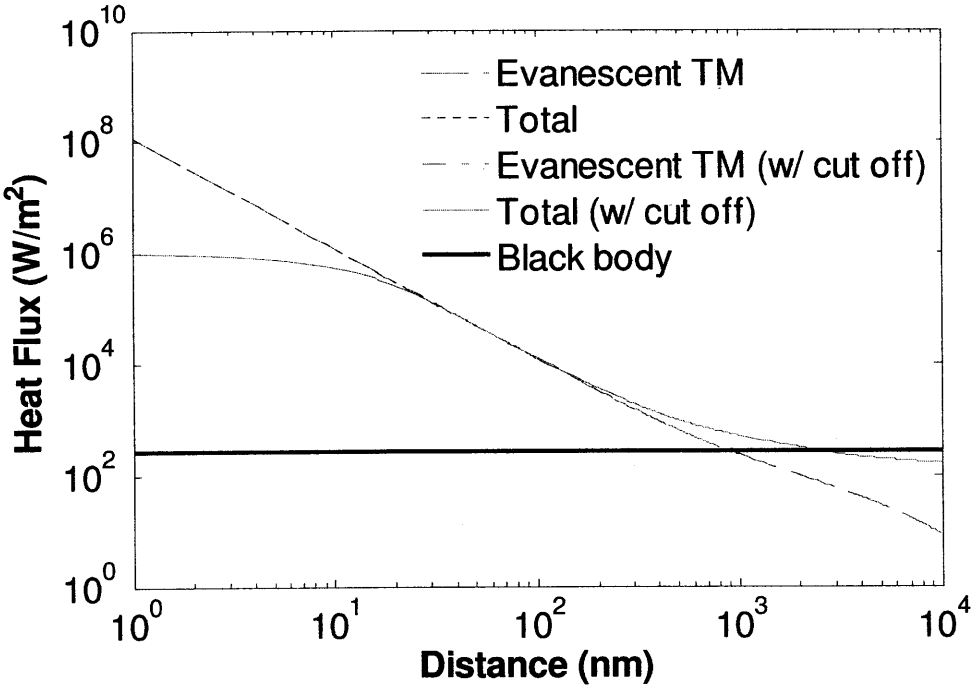

Figure 2.10 The expected saturation of the radiative heat transfer for very small separation distances resulting from the spatial dispersion of the dielectric constant.

Fig. 2.10 shows the expected saturation of the radiative heat transfer for very small separation distances resulting from the spatial dispersion of the dielectric constant. A cut-off value of the parallel wavevector of 10^8 (rad/m) is imposed in the simulation to illustrate the effect of spatial dispersion of the dielectric constant. This cut-off value leads to the saturation of the radiative heat transfer starting at ~30 nm separation distance. This cut-off value only influences the evanescent TM modes. The evanescent TE modes contribution remains constant as shown in Fig. 2.2, as the contribution from evanescent TE modes has parallel wavevectors much smaller than 10^8 (rad/m), illustrated in Fig. 2.5b.

2.3 Casimir Force between Two Parallel Plates

The quantification of the fluctuations of electromagnetic fields in vacuum which constitute the zero point energy generates forces. Two uncharged parallel plates are a typical example of this force. These two plates modify the boundary conditions of the fluctuations of the electromagnetic fields. It reduces the normal modes, which can occupy the space between two plates, and alters the zero point energy. The van der Waals force refers to a limit when the separation distances are smaller than the characteristic absorption wavelength. In this limit, the retardation effects are negligible. This theory was pioneered by London in 1930. The Casimir force refers to a limit when the separation distances are comparable or larger to the characteristic absorption wavelength. In this limit, the retardation effects are important. This force was first predicted by Hendrick Casimir in 1948 [57]. Previously, the van der Waals and Casimir forces were considered as two different forces rather than a single physical phenomenon at two different limiting cases.

The Casimir force has been proven to be a problem in nanoscale devices. This force is responsible for causing tiny devices to stick together. Since our experiment is performed at single nanometer separation distances, we need to assess how this force will interfere with our experiment.

Lifshitz [58] was the first to develop a unified theory of both the van der Waals and Casimir forces in 1955. Lifshitz's theory describes these forces as momentum transfer between media and treated the calculation based on Fluctuation Dissipation Theorem. For the case of two parallel plates as shown in Fig. 2.1, Casimir pressure is obtained by calculating the zz component of the Maxwell stress tensor at the interface between medium 1 and 0.

$$T_{zz} = \frac{1}{2}\left[\varepsilon\left(E_{\perp}^{2} - E_{z}^{2}\right) + \mu\left(H_{\perp}^{2} - H_{z}^{2}\right)\right] \tag{2.20}$$

Electric field and magnetic field can be obtained using dyadic Green's function following Eqs. (2.6) and (2.7). Through some mathematical manipulation the Casimir pressure can be calculated by the following expression.

$$P=\frac{\hbar}{2\pi^2c^3}\int_0^\infty\int_1^\infty p^2\xi^3\left\{\begin{array}{l}\left[\frac{(s_1+p)(s_2+p)}{(s_1-p)(s_2-p)}e^{2p\xi d/c}-1\right]^{-1}\\+\left[\frac{(s_1+p\varepsilon_1)(s_2+p\varepsilon_2)}{(s_1-p\varepsilon_1)(s_2-p\varepsilon_2)}e^{2p\xi d/c}-1\right]^{-1}\end{array}\right\}dpd\xi \qquad (2.21)$$

where $s_{1,2}=\sqrt{\varepsilon_{1,2}-1+p^2}$, and the dielectric constants are evaluated at imaginary frequencies $i\xi$ according to

$$\varepsilon(i\xi)=1+\frac{2}{\pi}\int_0^\infty\frac{\omega\varepsilon''(\omega)}{\omega^2+\xi^2}d\omega \qquad (2.22)$$

Eq. (2.21) is widely known as Lifshitz formula. Fig. 2.11 shows the Casimir pressure between two parallel plates calculated using the above formula.

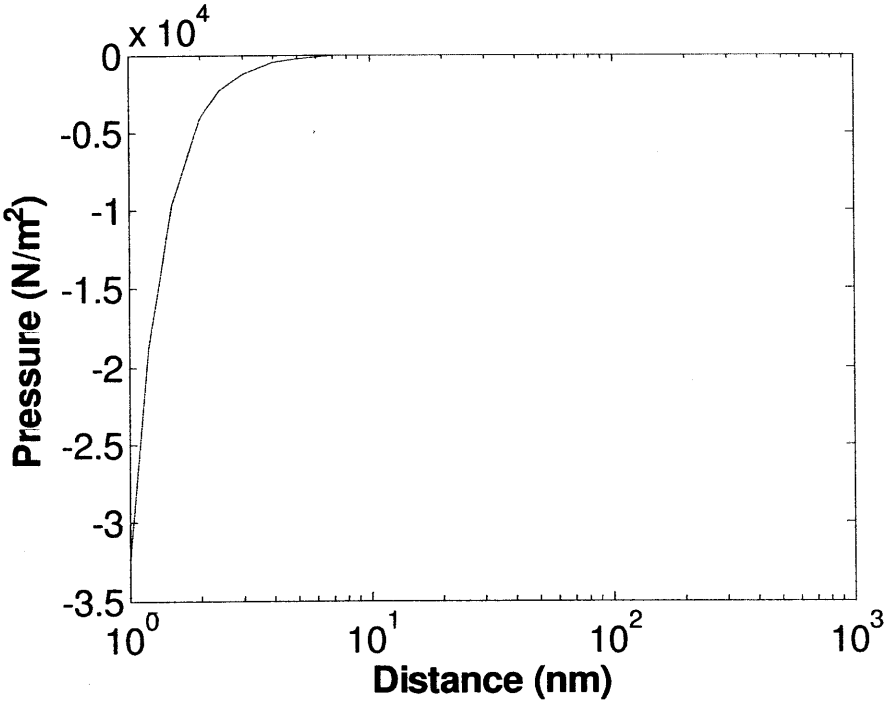

Figure 2.11 Casimir pressure between two parallel glass plates.

2.4 Proximity Force Theorem

In this experiment, we measure the near-field radiative transfer between a microsphere and a plate. Since there is no theoretical solution for the near-field radiative transfer between a sphere and a plate, we use proximity force theorem which is widely used to approximate the force between a sphere and a plate, to compare the experimental result

with the theoretical calculation. The sphere is considered very large relative to the separation distance that the curvature of the sphere changes very slowly. The curved surface is approximated by differential flat areas, as shown in Fig. 2.12.

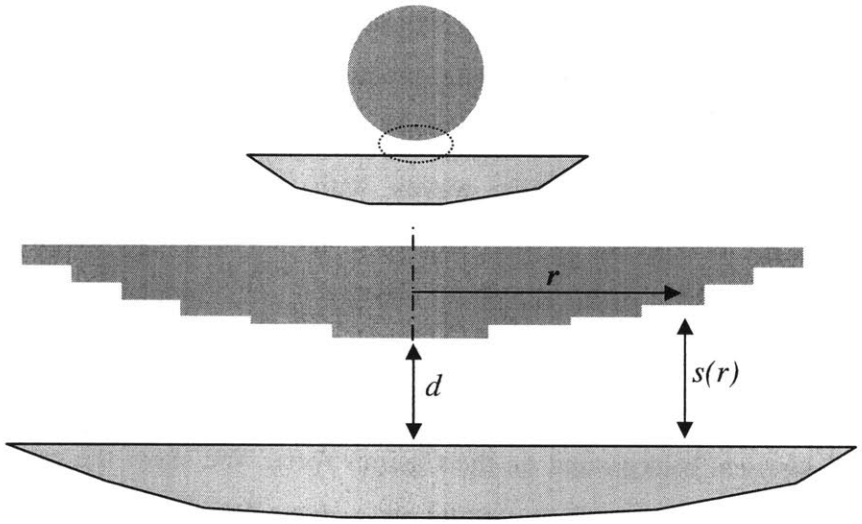

Figure 2.12 Proximity force theorem approximates the curved surface of the microsphere by differential flat surfaces.

The near-field radiative conductance between a sphere and a plate can be approximated by two parallel plates solution.

$$G_{near-field}^{sphere-plate}(d) = \int_{r=0}^{R} h_{near-field}^{plate-plate}(s(r)) 2\pi r dr \tag{2.24}$$

G is the radiative conductance, d is the separation distance between the sphere and the substrate, R is the radius of the sphere, h is the radiative heat transfer coefficient, and $s = d + R - \sqrt{R^2 - r^2}$ is the separation distance of between each differential plate and the substrate. The Casimir force between the sphere and the substrate is also approximated by the same procedure, simply replacing the radiative heat transfer coefficient h with the Casimir pressure, P.

2.5 Summary

We have provided a theoretical background on near-field thermal radiation. The theoretical foundation to calculate and analyze thermal radiative heat transfer between

two parallel plates is based on fluctuational electrodynamics. We present the calculation result of the radiative heat transfer between two plates for two different materials: glass which support surface waves, and silicon which does not. We also explain the reason for the divergence of the heat transfer as the separation distance becomes very small for a material which support surface waves. The explanation is then related to the concept of the dielectric constant. The local dielectric constant, which assumes a zero correlation length, implies that electromagnetic waves with any wavelength can exist and consequently to the divergence of the heat flux. To solve the problem, one needs to include a spatial dispersion of the dielectric constant in the calculation. Unfortunately, a lack of data on the spatial dispersion of the dielectric constant, especially for dielectrics such as glass, has prevented us from performing the calculation. We have briefly discussed a theoretical background on the Casimir force. We show the calculation result of the Casimir pressure between two parallel glass plates. We also provided the basic idea of the Proximity Force Theorem to compare the experimental result with the theoretical calculation.

Chapter 3

Experimental Investigation

This chapter presents the experimental setup and procedures that were used in this study. First, we will review previous experimental investigations. Then we will explain the basic concept of our experimental setup and procedures. Finally, we will emphasize problems encountered during experiments and attempts taken to solve them.

3.1 Previous Experimental Studies

Experimental studies on near-field radiation commenced in the late 1960's by Tien and co-workers [22, 23]. Domoto *et al.* [24] reported the first experimental work on near-field radiation. They measured radiative heat transfer between two parallel copper disks with separation gaps ranging from 2 mm to 10 μm at cryogenic temperatures (~10 K). The temperature of the emitter was maintained at 10 K and 15.1 K, while the receiver was maintained at approximately 4.5 K. In this temperature range, near-field effects can be observed at large separation gaps (~100 um). Large separation gaps significantly reduce the difficulty of aligning two parallel plates. In this first effort, even though the near-field mediated heat transfer measured was greater than that of the far field, the measured heat flux only made up 3% of the total energy transfer between ideal blackbodies.

Another early experimental work on near-field thermal radiation was carried out by Hargreaves [25]. He measured the radiative heat transfer between two optically flat surfaces coated with 1000 Å thick Chromium. The temperatures of the plates were maintained at 323 K and 306 K for the emitter and cold side, respectively. In this temperature range near-field effect can be observed as of ~10 μm. He pushed the separation gap down to as low as 1.5 μm and was able to maintain both plates parallel at such small separation gaps by measuring the capacitance and the interference pattern on

the chromium surfaces. At a 1.5 μm vacuum gap, the near-field heat transfer at room temperature was 5 times greater compared to that in the far field. However, the measured heat flux was still only 40% of that between two blackbodies.

20 years later the next reported experiment on near-field radiation was performed by Xu *et al.* [26]. A squeezed indium needle and a flat gold surface of a planar thermocouple were used as two parallel plates. The temperature difference between the needle and the thermocouple was in the range of 40 K, while the thermocouple junction was maintained at room temperature. While the gap was made smaller than 100 nm, the results remained inconclusive, mainly due to the sensitivity of the experimental setup.

In 2005 Kittel *et al.* [27] measured the heat transfer between the tip of a scanning thermal microscope and a gold (Au) or gallium nitride (GaN) surface at separation gaps between 100 nm and 1 nm. The temperature of the sample was lowered down to 100 K, while the tip was maintained at room temperature, establishing a 200 K temperature difference between the tip and the sample. Their results clearly showed heat transfer enhancement at small gaps and agreed well with predicted values for separation gaps larger than 10 nm. For separation gaps less than 10 nm the measured heat transfer saturated which differed from the divergent behavior seen in the predicted results. The authors speculated that the observed saturation was due to the spatial dependence of the dielectric constant. By replacing a flat plate with a STM tip, which is assumed to behave like a point-like dipole, the problem of parallelism between two plates is eliminated. Other concerns such as the cleanliness of the surface and the surface roughness are also minimized because of the small surface area of the tip. However, several drawbacks should be noted. The geometry of the tip is difficult to model thus any comparisons between theoretical and experimental results inherently include more uncertainty. The magnitude of the near-field radiative transfer is also much smaller due to the small surface area of the tip. This makes the measurement more challenging as the sensitivity of the experiment was not sufficient. The far-field radiative transfer between the tip holder, which has a large surface area, and the sample most likely interfered with the near-field radiation between the tip and the sample. Despite all these disadvantages, this is the only near-field thermal radiation measurement which observed a saturation of the

heat transfer when the separation gap became very small. This again is suspected to occur because of the spatial dispersion of the dielectric constant.

In 2008, Hu *et al.* [29] measured the radiative heat flux between two parallel glass substrates. The separation was maintained by using small polystyrene spheres. The separation is limited to 1 μm due to the diameter of the spheres. Other disadvantages of this experiment are the difficulties of aligning two parallel plates and ensuring that both surfaces do not make any physical contact. These results clearly showed that the radiative heat flux exceeds Plank's law of blackbody radiation and were the first to do so. The primary contribution to the heat transfer is attributed to surface phonon polaritons.

Narayanaswamy *et al.* [28] developed a new technique to measure near-field thermal radiation between a microsphere and a flat surface using a bi-material cantilever. This technique elegantly solves the parallelism issues found in two parallel plates case, while at the same time keeping the magnitude of the heat transfer large enough to be clearly observed. Using the same experimental setup, Shen *et al.* [30] successfully demonstrated that the near-field radiative heat transfer between polar dielectric materials can exceed Planck's blackbody radiation by three orders of magnitude when separation gaps are as small as 30 nm. Again this enhancement to the influence surface phonon polaritons at these length scales.

Rosseau *et al.* [31] measured the radiative transfer between a glass microsphere and a glass substrate using a similar experimental setup used by Shen *et al.* [30] with two modifications. The first modification is to heat the substrate instead of the cantilever. The other modification is to use a fiber interferometer technique to measure the cantilever deflection. These modifications actually caused more problems rather than improving the experiment. The heated substrate will transfer heat not only to the sphere, but also to the cantilever. The deflection of the cantilever is then not only due to near-field effects between the sphere and the substrate but also due to far-field radiative transfer between the substrate and the cantilever. By placing a fiber near the cantilever to measure its deflection, radiative transfer between the cantilever and the fiber is also very likely to occur. Instead of isolating the measurement between the substrate and the sphere, the placement of the fiber near the cantilever complicates the measurement by introducing a third emitting body. Another drawback is the introduction of a calibration factor which

depends on an unreliable assumption of the emissivity of the silica sphere. They also included the far-field contribution through calculation. This calculation does not seem accurate since they only include the radiative exchange between the sphere and the substrate while in reality the size of the sphere is much smaller compared to the cantilever. Despite all these disadvantages, they report the radiative transfer measurement, including far-field contribution, for separation distances between 30 nm and 2.5 μm. Their results fit the theoretical calculation based on the Proximity Force Approximation very well. However, since the experimental results depend on the proportionality factor that they introduced based on an unreliable analysis, the agreement between the experimental data and the theoretical calculation is questionable.

3.2 Experimental Setup

The near-field thermal radiation experimental setup in the Nanoengineering Group at MIT (Rohsenow Kendall Heat and Mass Transfer Laboratory) was first set up by Arvind Narayanaswmay during his Ph.D. thesis in the Department of Mechanical Engineering. This experimental setup was then refined and used by Sheng Shen as a part of his Ph.D. work in the same group. In the following, we merely highlight the basic principle of the experiment and refer the reader to Narayanaswamy's and Shen's Ph.D. thesis for a comprehensive description of the setup [57, 52]. The most significant change made in this study is to replace the piezoelectric motion control by more accurate one (Nano OP series, Mad City Lab). This gives us the ability to reduce the gap size to 1 nm.

A schematic of experimental setup is given in Fig. 3.1. An incident laser beam is focused onto a bi-material cantilever with a microsphere attached on its tip by using a focusing lens and an adjustable mirror. Part of the laser power is absorbed by the cantilever, thus providing a temperature difference between the microsphere and the substrate which is passively maintained at room temperature. The reflected portion of the laser power is directed onto a four quadrant position sensing detector (PSD), which is used to measure the displacement of the reflected beam. A position sensing amplifier is used to convert the output of the PSD into X and Y difference signals, corresponding to the position of the laser spot on the PSD and a sum signal corresponding to the laser power incident on the PSD. The experimental setup is placed inside a vacuum chamber

and the measurement is done under vacuum conditions at 10^{-3} Pa to avoid any convective heat transfer effects.

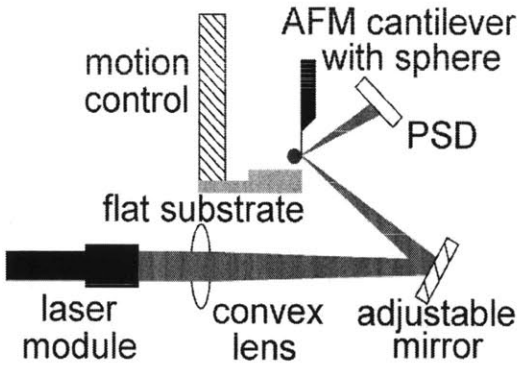

Figure 3.1 Schematic of the experimental setup. The laser beam deflected from the adjustable mirror onto the cantilever is the "incident beam" and the beam reflected from the cantilever to the PSD is the "reflected beam." The experimental setup consists of a laser diode module, a focusing lens and a mirror to direct the laser beam onto the cantilever, the AFM cantilever with a microsphere attached on its tip, a substrate mounted on a piezoelectric motor, and a position sensing detector (PSD). All of these components are mounted on a standard aluminum optical breadboard. Figure adapted from [57].

The bi-material cantilever is the central element of the experimental setup. It is used as both temperature and heat transfer sensor, extracted from the bending of the cantilever resulting from the difference in thermal expansion of the two materials. A commercial triangular silicon nitride AFM cantilever is used for this purpose. The AFM cantilever is made of 450 nm thick of Si_3N_4 coated with 70 nm gold film. Its effective length is 200 μm. This cantilever was also used by Shen *et al.* [30]. Based on the beam theory [59], the deflection of a bi-material cantilever with two different thermal expansion coefficients follows

$$\frac{d^2Z}{dx^2} = 6(\gamma_2 - \gamma_1)\frac{t_1 + t_2}{t_1 t_2 K}[T(x) - T_0] \tag{3.1}$$

where $Z(x)$ is the vertical deflection at location x, γ is the thermal expansion coefficient, K is a constant defined by the thickness ratio and the Young's modulus of the layers, t is the

thickness of the layers, $T(x)$ is the temperature distribution along the cantilever, and T_0 the reference temperature at zero deflection. In this case T_0 is room temperature.

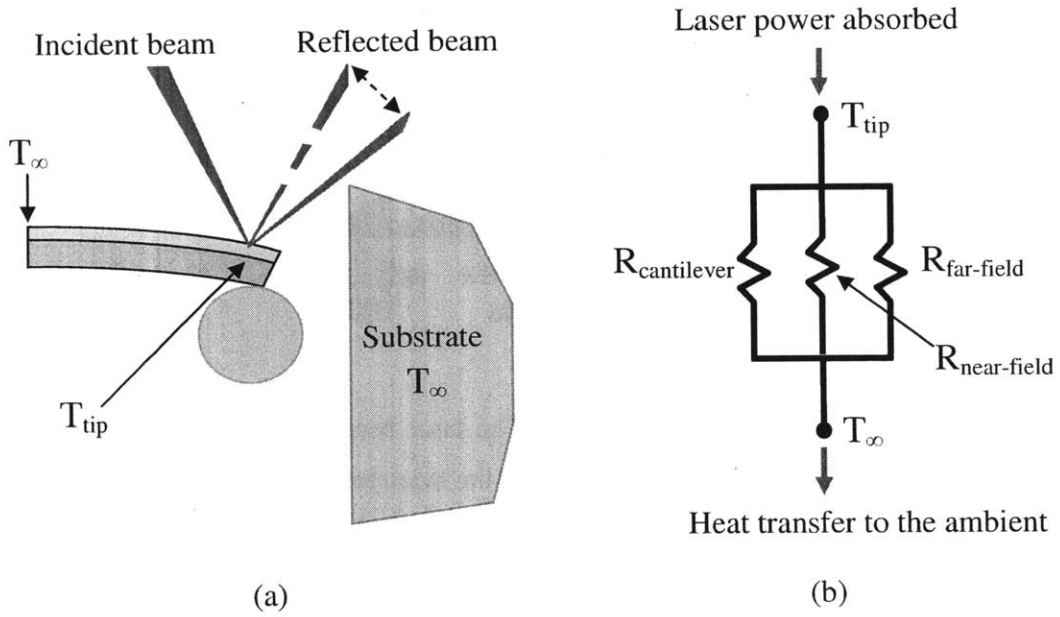

Figure 3.2 (a) Bending of the cantilever as the substrate moves towards the microsphere. (b) Equivalent thermal circuit.

Fig. 3.2 illustrates the basic idea of the experimental setup. Fig. 3.2a shows the bending of the cantilever as the substrate moves toward the microsphere. The corresponding thermal circuit is given in Fig. 3.2b. The temperature of the cantilever tip can be written as

$$T_{tip} = \left[\frac{1}{R_{near-field}} + \frac{1}{R_{far-field}} + \frac{1}{R_{cantilever}} \right]^{-1} P + T_{\infty} \tag{3.2}$$

P is the laser power absorbed by the cantilever, $R_{near\text{-}field}$ is the near-field radiation thermal resistance between the sphere and the substrate, $R_{far\text{-}field}$ is the far-field radiation thermal resistance between the sphere and the cantilever to the surroundings, and $G_{cantilever}$ is the thermal conductance of the cantilever. The deflection of the cantilever is very small such that the amount of the laser power absorbed by the cantilever tip, P, is assumed to be constant during the experiment. The cantilever tip is assumed to be at the same temperature as the sphere, since the near-field thermal radiative heat transfer from

the microsphere to the substrate is very small (~100 nW), compared to the conduction through the cantilever (~100 μW).

The experiment is done based on the following idea. $R_{near\text{-}field}$ decreases as the separation gap between the sphere and the substrate becomes smaller because the near-field thermal radiation component increases. As a result the temperature T_{tip} will decrease to balance the heat flow following Eq. (3.2). This temperature change will cause the cantilever to bend upwards and change the position of the reflected beam on the PSD.

Here, we emphasize that our experimental setup only measures near-field radiative transfer and does not measure far-field radiative transfer. $R_{far\text{-}field}$ is modeled as a small sphere in a large enclosure [1] and remained constant during the measurement since the separation distance between the sphere and the substrate only changed on the order of ~10 μm. The measured near-field radiative transfer is on the order of ~100 nW, corresponding to a ~ 10^{-2} K temperature change of the sphere. A ~10^{-2} K temperature change of the sphere corresponds to ~ 1 nW change in the far-field radiation loss from the sphere, which is much smaller than the measured near-field radiative transfer. Hence, the deflection of the cantilever is only due to the near-field effect. We also emphasize that our experimental setup does not suffer from the drawbacks seen by Rosseau *et al.* [31]. We heat the sphere, not the substrate, by shining a laser on the tip of the cantilever. Therefore, the heat transfer between the substrate and the cantilever is minimized and becomes negligible when compared to the near-field radiative transfer between the sphere and the substrate. Compared to their calibration method, our calibration method is independent of any assumption on the emissivity of the silica sphere. Hence, our measurement results are free from the uncertainty introduced by the emissivity of the silica sphere.

3.3 Calibration Process

Through a set of calibration steps [60], the displacement of the reflected laser beam on the PSD is converted to a magnitude of the near-field thermal radiative transfer between the microsphere and the substrate.

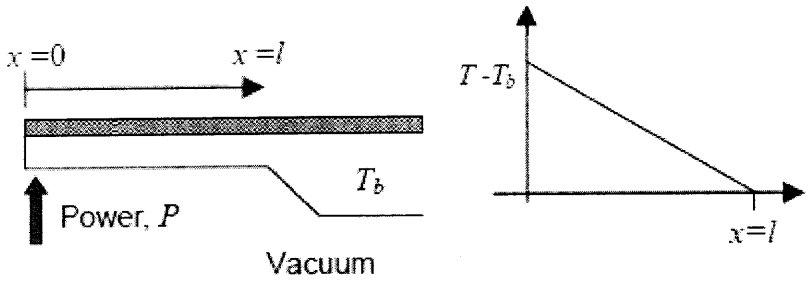

Figure 3.3 Schematic of the cantilever with power input on its tip in vacuum and its corresponding temperature profile. Adapted from [60].

The first necessary calibration is the power calibration. The temperature profile of the cantilever under vacuum conditions with a point-like power input on its tip, as shown in Fig. 3.3, can be written as

$$T(x)-T_b=\left(1-\frac{x}{l}\right)\frac{P}{G} \tag{3.3}$$

where P is the laser power absorbed by the cantilever tip, G is the effective thermal conductance of the cantilever, l is the effective length of the cantilever, and T_b is the base temperature. The effect of the far-field radiation is very small since $R_{far\text{-}field}$ is very large compare to $R_{cantilever}$. Based on this temperature profile, the slope of the cantilever tip can be determined from Eq. (3.1).

$$\frac{dZ(0)}{dx}=6H\left\{-\frac{lP}{2G}-T_b l+T_0 l\right\} \tag{3.4}$$

Since in this case $T_b = T_0$, Eq. (3.4) reduces to

$$\frac{dZ(0)}{dx}=-\frac{3lPH}{G} \tag{3.5}$$

where $H=(\gamma_2-\gamma_1)(t_2-t_1)/t_2t_1K$, is a constant obtained from Eq. (3.1). The slope of the cantilever tip is approximately equal to half of the position change of the reflected beam on the PSD,

$$\frac{dZ(0)}{dx}=0.5\frac{\Delta d}{s} \tag{3.6}$$

where Δd is the displacement of the reflected beam on the PSD and the actual signal measured, and s is the distance between the cantilever tip and the PSD.

The sensitivity of the displacement of the reflected beam on the PSD to the absorbed power is given by

$$S_p = \frac{\partial(\Delta d)}{\partial P} = -\frac{6slH}{G} \tag{3.7}$$

This calibration is carried out by measuring the displacement of the reflected laser beam on the PSD in response to different laser powers absorbed at the tip of the cantilever under vacuum.

The second necessary calibration is the temperature calibration. The temperature of the cantilever tip can be calculated using Eq. (3.3) with knowledge of G. Since the properties of the cantilever depend on its dimensions, the effective conductance of the cantilever G needs to be determined experimentally [60]. In order to obtain the value of G another calibration needs to be performed.

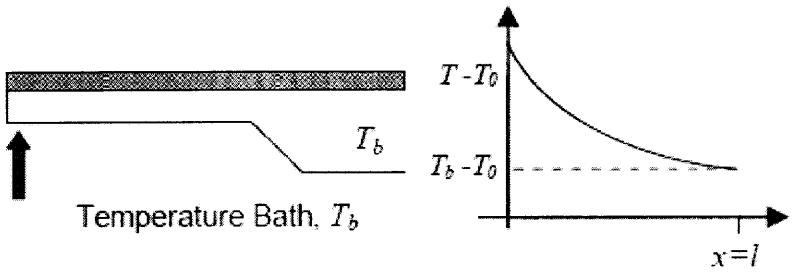

Figure 3.4 Schematic of the cantilever with power input on its tip in ambient environment and its corresponding temperature profile. Adapted from [60].

Since the thickness of the cantilever is very thin compared to its length, the cantilever can be treated as a fin. The temperature profile of the fin in ambient environment at temperature T_b is shown in Fig. 3.4. The base temperature is assumed to have the same temperature. The temperature profile as a function of position can be written as

$$T(x) - T_b = \frac{P\sinh[\beta(l-x)]}{G\beta l\cosh(\beta l)} \tag{3.8}$$

where

$$\beta = \sqrt{\frac{2h(w+t_1+t_2)}{lG}} \tag{3.9}$$

Based on the temperature profile above, the slope of the cantilever tip can be determined from Eq. (3.1).

$$\frac{dZ(0)}{dx} = -6H\left\{(T_b - T_0)l + \frac{P[1-\sec h(\beta l)]}{\beta^2 l}\right\} \tag{3.10}$$

For the purposes of this calibration, the second term in the Eq. (3.10) is not important since it is not a function of T_b. Using Eq. (3.6), the sensitivity of the displacement of the reflected laser beam on the PSD due to ambient temperature variation is

$$S_T = \frac{\partial(\Delta d)}{\partial T_b} = -12sHl \tag{3.11}$$

Using Eqs. (3.7) and (3.11), the effective conductance of the cantilever is

$$G = \frac{S_T}{2S_P} \tag{3.12}$$

To carry out this calibration the experimental setup is placed inside the vacuum chamber. A hair dryer is used to increase the air temperature inside the vacuum chamber. After the temperature inside the chamber reaches a certain value, the hair dryer is turned off and the experimental setup is naturally let to cool down. A K-type thermocouple is attached to the cantilever chip to measure the change in ambient temperature while the difference signal is recorded as a function of the temperature change.

After the air inside the vacuum chamber is heated using a hair dryer, the air inside the chamber is left to stabilize. This waiting time can be long enough for some thermal drift to interfere with the measurement setup. The variation in calibration results arises due to different degrees of the thermal drift, as illustrated in Fig. 3.5. The sensitivity to the ambient temperature variation is -0.346 V/C for minimum drift, and -0.135 V/C for maximum drift.

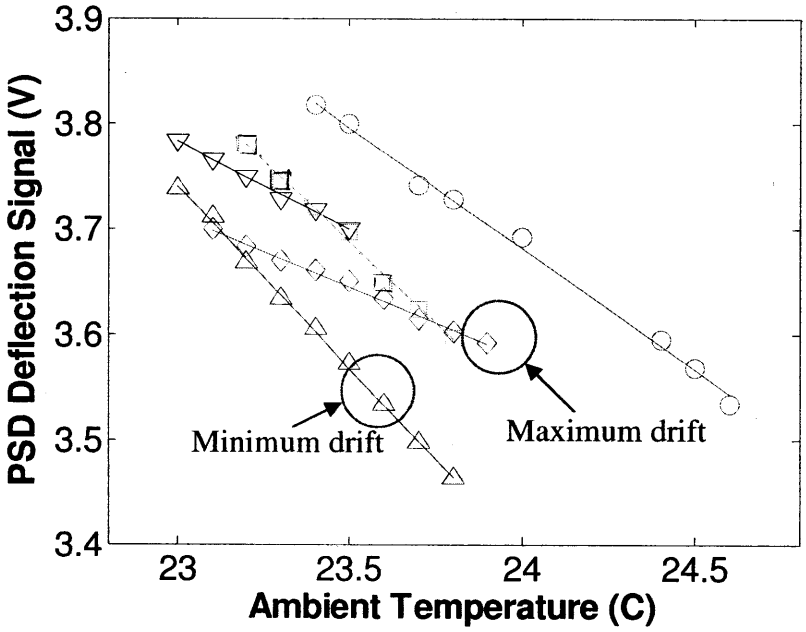

Figure 3.5 Deflection of the cantilever as response to ambient temperature variation for five trials.

To solve this problem, instead of varying the ambient temperature, we propose to vary the temperature of the cantilever base in vacuum environment. An RTD heater is attached on the copper plate to actively control the temperature of the cantilever base. The difference signal is then recorded as a function of the temperature of the cantilever base.

For this case, the slope of the cantilever tip is given by Eq. (3.4). Following the same procedure as previously, the sensitivity of the displacement of the reflected beam on the PSD to the base temperature is

$$S_T = \frac{\partial(\Delta d)}{\partial T_b} = -12sHl \tag{3.13}$$

The same result as Eq. (3.11) is obtained.

This method eliminates the stability problem suffered by the previously introduced calibration method. Fig. 3.6 shows the calibration results as response to the base temperature variation for three different runs. All of them give the same sensitivity: -0.351 V/C, -0.352 V/C, and -0.356 V/C. Note that the sensitivity of the cantilever as response to the ambient temperature variation in the case for minimum drift gives the same value (-0.346 V/C) with the sensitivity of the cantilever as response to the base

temperature variation (0.351 V/C, -0.352 V/C, and -0.356 V/C). This confirms the theoretical analysis that both methods should give the same results.

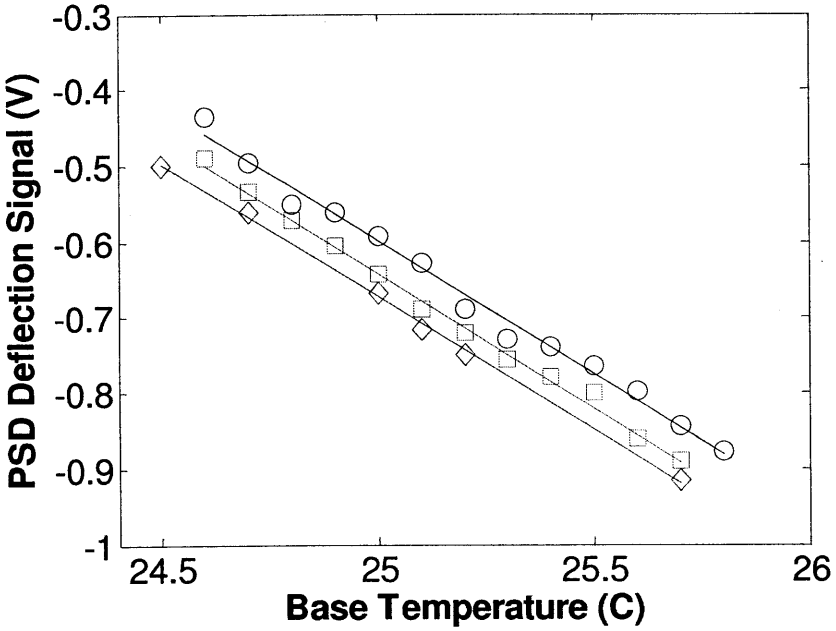

Figure 3.6 Deflection of the cantilever as a response to the base temperature variation under vacuum conditions for three different trials.

3.4 Improvements made to the experimental setup

Through our experience working on the experimental setup, we found that several things could be done to improve it. These improvements include using an etched silicon surface to place microspheres on before attaching them to the cantilever, a better system alignment, smoother surface roughness of the microspheres, and the influence of the force at very small gaps.

3.4.1 Attaching the microsphere to the cantilever tip

We follow the method introduced by Narayanaswamy [58] to attach a microsphere onto the AFM cantilever tip. The AFM cantilever chip is first attached to a copper base using silver epoxy to make its handling easier. The tip of the AFM cantilever is then dipped into UV glue. Some microspheres are placed on a glass slide and the AFM cantilever is

controlled with a micro manipulator to attach a microsphere onto the cantilever tip. After curing the glue under UV light for a minute, the AFM cantilever can be displaced with a microsphere attached on its tip. Further curing with the UV light is needed to make sure that the glue is perfectly hardened.

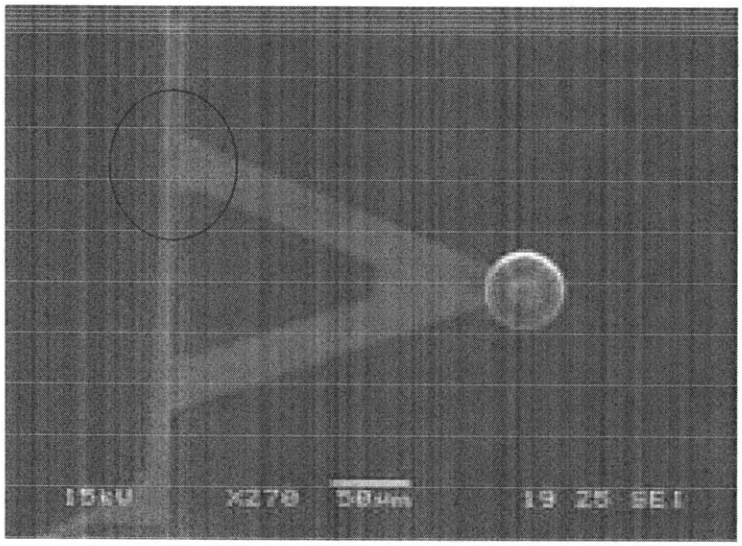

Figure 3.7 Defects occurring when attaching a microsphere to the AFM cantilever.

From our experience, we found that the force between the microspheres and the glass slide where they are placed on is quite strong. Sometimes the force is stronger than the adhesive force of the UV glue. On a rare occasion this force caused a fracture on the cantilever base, as shown in Fig. 3.7, since the cantilever base experiences the largest stress because of its length and stress concentration. To avoid this problem, instead of placing microspheres on a glass slide, we use an etched silicon surface, shown in Fig. 3.8 below. With less contact area, the surface and contact forces are smaller and the attachment process hence becomes much easier.

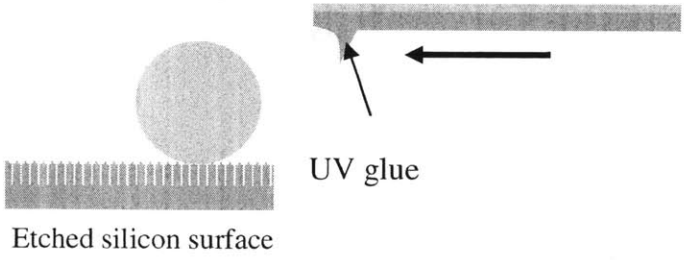

Figure 3.8 Schematic of the etched silicon surface to place microspheres onto during the attachment process. Figure inspired by [58].

3.4.2 Cantilever Alignment

As pointed out already by Narayanaswamy [58], the alignment of the cantilever is one of the challenges in this experimental setup. This is caused by the position of the cantilever and the sphere relative to the edge of the substrate as shown in Fig. 3.9. The sphere should ideally be positioned deep enough from the edge of the substrate for the sphere-plate approximation to be valid, as shown in Fig. 3.9a. If the sphere is positioned at the edge of the substrate, as shown in Fig. 3.9b, then the sphere-plate approximation does not hold anymore because the upper side of the sphere will see the edge of the substrate. This misalignment also introduces unbalanced forces between the upper and lower side of the sphere. The bending caused by this unbalanced force will then consequentially interfere with the measurement.

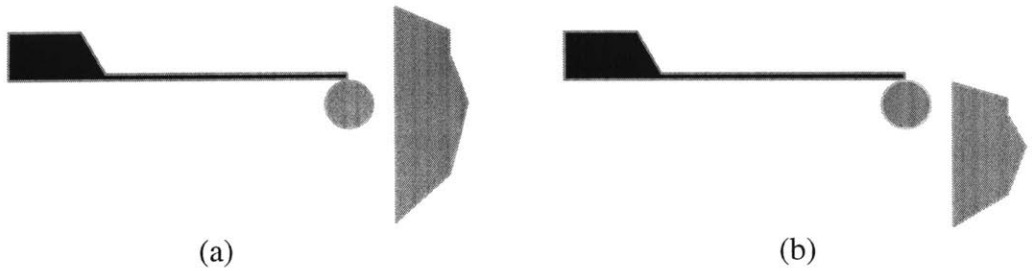

Figure 3.9 Position of the cantilever and the microsphere relative to the substrate. Figure inspired by [58].

The other challenge in the setup is laser alignment. As the sphere location is farther inward with respect to the edge of the substrate, as shown in Fig. 3.9a, the incident laser beam needs to have a smaller angle of incidence. Otherwise, the incident laser beam is blocked by the substrate as shown in Fig. 3.10 below.

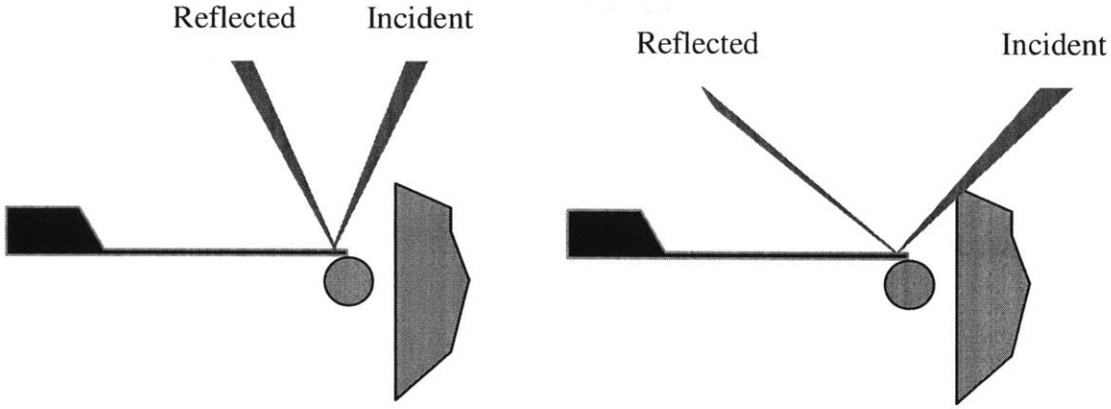

Figure 3.10 Restriction on the positioning of the cantilever and the substrate due to obstruction of the laser beam. Figure inspired by [58].

To solve this problem, we need to position the optical components of the experimental setup and make sure that the angle of incidence to be as small as possible. Fig. 3.11 shows the experimental setup.

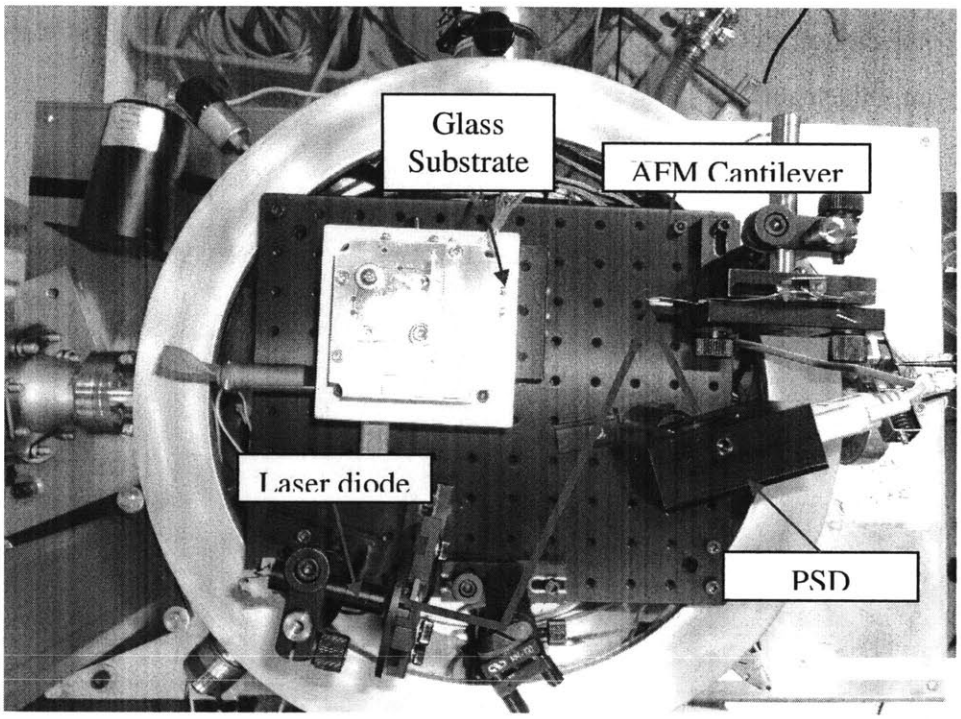

Figure 3.11 The near-field radiation experimental setup.

3.4.3 Microsphere Surface Roughness

The biggest challenge in the experiment is the surface roughness of the microsphere. While we aim to decrease the separation distance between the microsphere and the substrate below 30 nm, AFM analysis shows that the surface roughness of the microsphere itself is about 40 nm, while the roughness of the substrate is in the range of 4 nm.

The silica microspheres are made by forming liquid droplets (thermal plasma) of SiO_2. These droplets are then cooled in another immiscible liquid. The spherical shape is formed due to surface tension. The microspheres are purchased from Corpuscular Inc. They claim that the surface roughness quality cannot be improved. According to the company this surface roughness is the best possible result from the melting process. Despite their claim, we still tried to improve the surface roughness by heating the microspheres near their reflow temperature. The results are quiet promising as shown in Fig. 3.12. The roughness of the microspheres after an annealing step at 500°C for 30 minutes appears to improve as can be seen in the SEM images. Further experiments need to be carried though out to find the optimal annealing temperature and duration which gives the smoothest surface.

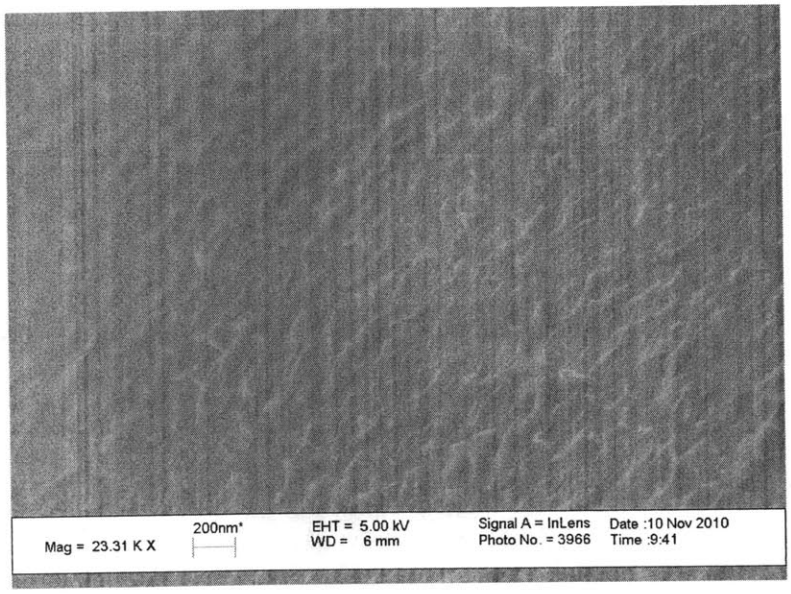

(a)

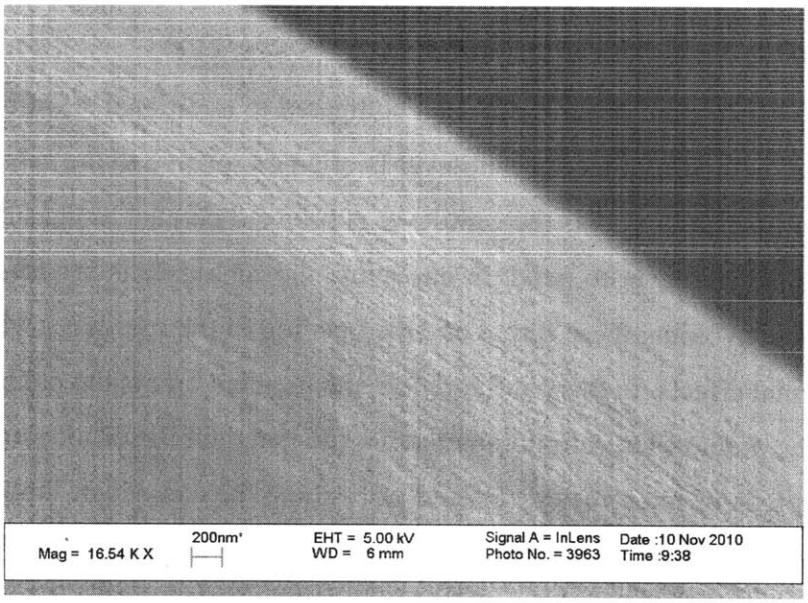

(b)

Figure 3.12 (a) SEM picture of the microsphere surface before and (b) after annealing at 500°C for 30 minutes.

We also try to polish the microspheres by using a sonicator. The results show that the surface roughness becomes smoother even though the microspheres have many craters, probably resulting from the collision with other spheres. The result is shown in Fig. 3.13 below.

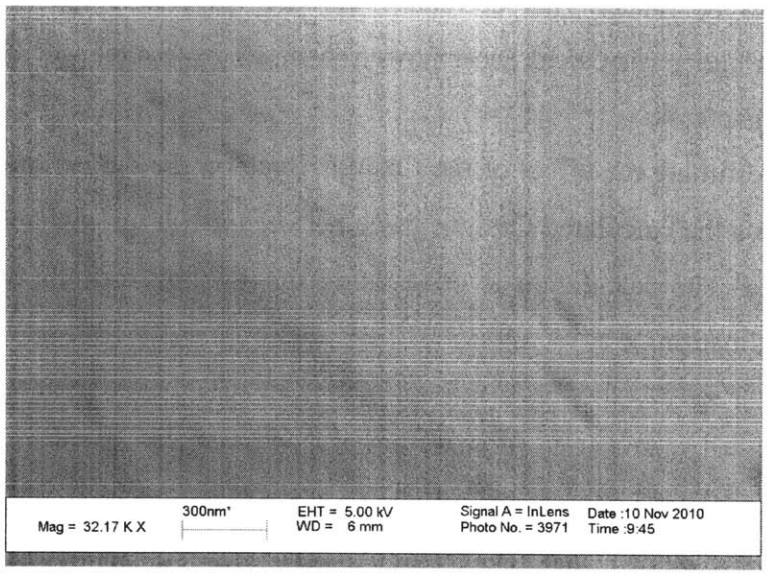

Figure 3.13 SEM picture of the microsphere surface after sonication for three days.

3.4.4 Force

The present experimental setup is different compared to traditional AFM or Casimir force measurements in the way that the cantilever is oriented relative to the substrate. In AFMs or Casimir force measurements the cantilever is oriented parallel to the substrate. Surface forces cause the cantilever to bend. In our setup, the cantilever is oriented perpendicular to the substrate, avoiding these forces and the bending of the cantilever will purely be the result of thermal effects. In this configuration, the moment arm is the radius of the sphere, which is in the order of tens of micrometer, not the length of the cantilever which is in the order of hundreds of micrometer. Instead of bending the cantilever, these surface forces will now tend to elongate the cantilever. When the forces are small, the elongation of the cantilever is expected to be very small and the resulting deflection of the cantilever due to these forces is expected to be negligible. This assumption above might not be true though for small separation gaps since the electrostatic force is proportional to $1/d^2$, and the Casimir force is proportional to $1/d^3$. The electrostatic force can be caused by charge accumulation on the sphere and the substrate, as well as the external field from the piezo motion control stage, the motor, and the wiring. The electrostatic force is minimized by grounding the tip and using shielded cables to isolate the field. To exclude the deflection of the cantilever due to the force, a correction to the measured deflection signal from the force needs to be made. This correction for the force is obtained by carrying out measurements under very weak laser power. A detail explanation of this correction can be found in Chapter 4.

Here, we estimate the effect of the Casimir force on the deflection of the cantilever. Fig. 3.14 shows the calculated Casimir force between a 100 μm silica microsphere and a glass substrate. The calculation is done using the Lifshitz formula and the Proximity Force Approximation.

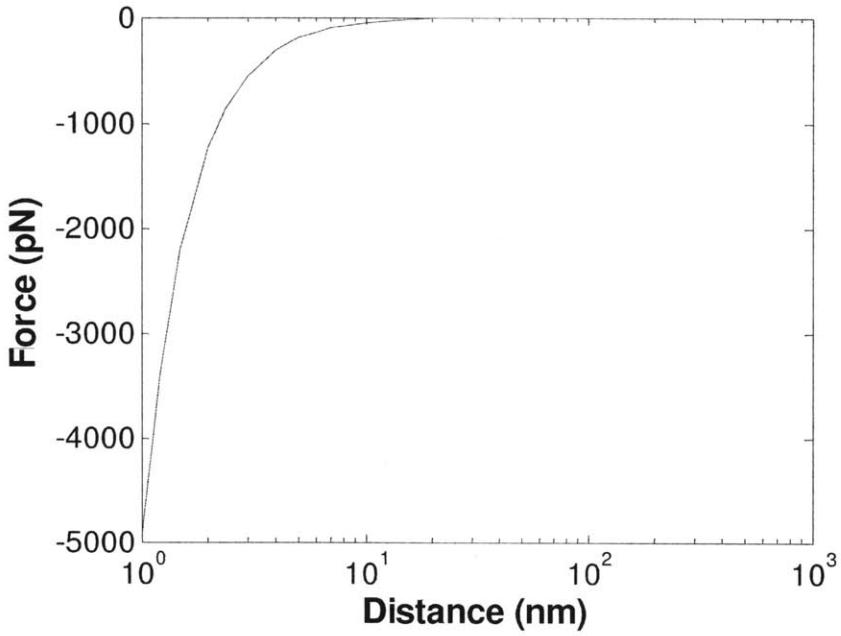

Figure 3.14 Casimir force calculation between a silica microsphere of 100 μm diameter and a glass substrate as function of gap separation.

Solid mechanics theory is used to estimate the deflection of the cantilever resulting from the Casimir force between the microsphere and the substrate. We model this problem as a beam with constant moment [61].

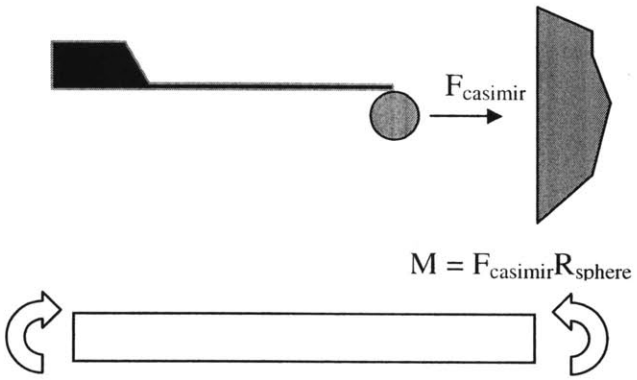

Figure 3.15 Schematic analysis of the bending of the cantilever resulting from the Casimir force.

The slope of the cantilever tip can be calculated by [61],

$$EI\frac{dZ}{dx} = Mx \tag{3.14}$$

E is elastic modulus, I is the moment of inertia and M is the bending moment. The elastic modulus of Au and Si_3N_4 are 82 GPa and 317 GPa, respectively. Since the effective elastic modulus for the cantilever is not known, the elastic modulus of Au is used as the upper limit. Fig. 3.17 presents an estimation of the deflection of the cantilever tip resulting from the Casimir force between the microsphere and the substrate.

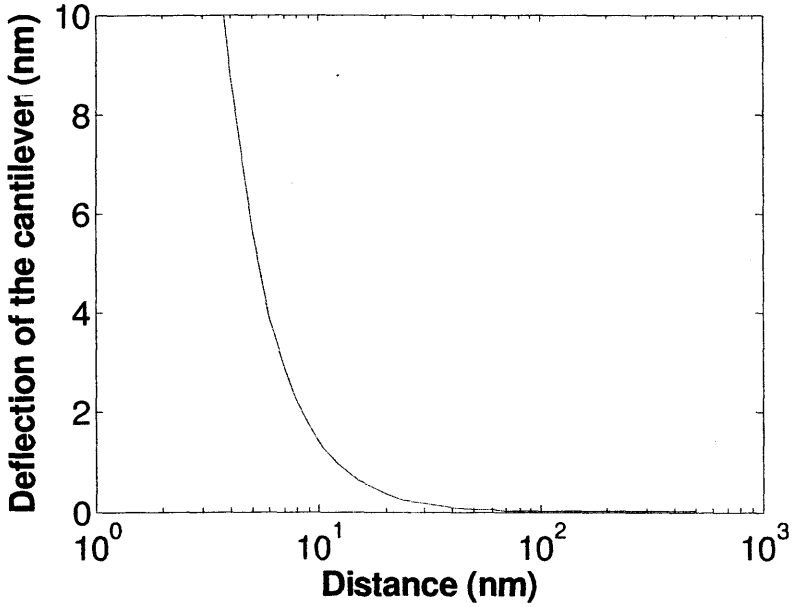

Figure 3.16 The deflection of the cantilever tip resulting from the Casimir force as a function of separation distance.

3.5 Summary

An overview of the near-field thermal radiation experimental setup has been provided. We refer the reader to Narayanaswamy's and Shen's Ph.D. thesis for a comprehensive description of the setup [57, 52]. We proposed a new temperature calibration procedure and showed that this procedure is more repeatable compared to the previous one. We also made several improvements on the experimental procedures and setup. These improvements include using an etched silicon surface to place microspheres on before attaching them to the cantilever, and a better system for alignment. We also tried to reduce the surface roughness of the microspheres, thus making them smoother. The results are promising but further trial needs to be carried out. We then estimated the effect

of the Casimir force on the measurement at very small gaps. The results will be compared with the force calibration in Chapter 4.

Chapter 4

Experimental Results and Discussions

In this chapter, preliminary experimental results of the near-field radiative heat transfer between a silica microsphere with a 100 μm diameter and a glass substrate at separation distances smaller than 30 nm are presented. We also measure the near-field radiative heat transfer at different temperatures differences. The temperature of the sphere can be varied by varying the laser power following Eq. (3.3), while the temperature of the substrate is passively maintained at room temperature. The experimental results are then fitted with the theoretical calculation.

4.1 Experimental Results

Fig. 4.1 shows typical raw data of the measurements. As the separation distance between the silica sphere and the glass plate becomes smaller, the radiative heat transfer increases, indicated by the change of the PSD difference signal. Contact is established when the PSD difference signal changes abruptly. The sharp change in difference signal indicates that the cantilever does not bend under the influence of thermal effects, but because of the contact force between the sphere and the substrate. Contact is the reference point for zero separation distance between the sphere and the substrate. The raw data is then processed by relating the recorded separation gaps with the zero reference point and converting the PSD difference signal into radiative heat transfer.

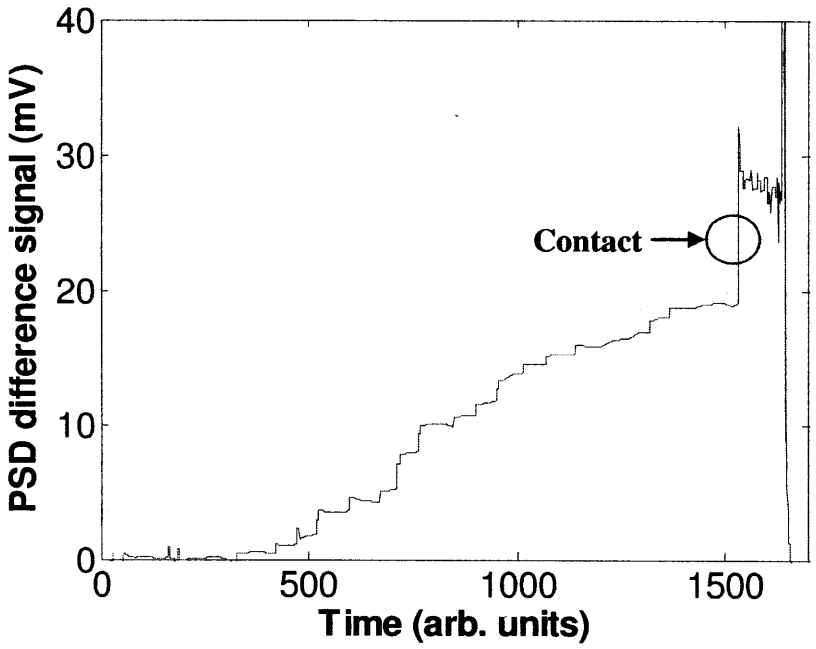

Figure 4.1 Typical raw data. The contact between the sphere and the substrate is reached as the PSD difference signal experiences an abrupt change.

To extract near-field radiative heat transfer data, a correction to the measured deflection signal from the force needs to be made. This correction for the force is obtained by carrying out measurements under very weak laser power. Under very weak laser power, the temperature difference between the sphere and the substrate is expected to be very small. Fig. 4.2(a) shows the extracted PSD signals for four different laser powers. Fig. 4.2(b) shows the corresponding deflection of the cantilever. The force correction is done by subtracting the experimental output with the very weak laser power signal.

Through the calibration process, the sensitivity S_P for the used cantilever was found to be S_P = 0.024 V/μW ($d(\Delta d)/dP$ = 12μm/μW, $d(dZ(0)/dx)/dP = 6 \times 10^{-5}$ (rad/μW), dZ(0)/dP = 4 nm/μW), and S_T = 0.35 V/K ($d(\Delta d)/dT$ = 180μm/K, $d(dZ(0)/dx)/dT = 9 \times 10^{-4}$ (rad/K), $dZ(0)/dT$ = 60 nm/K). Using Eq. (3.12), the effective conductance of the cantilever extracted was 7.5 μW/K. This value is very close with to what was obtained by Shen *et al.* [30] (7.91 μW/K). This result confirms the repeatability of our calibration processes. The theoretical value of the conductance of the cantilever is estimated using

the dimensions of the cantilever and assuming the thermal conductivities of the Si_3N_4 and Au films to be 2.5 [63] and 190 W/m/K [64], respectively. The theoretical value of the conductance is estimated to be around 5.88 μW/K. The thermal conductivities of Si_3N_4 and Au films used here are smaller than their bulk values due to grain-boundary and boundary scatterings. The agreement between measurement and estimation is reasonable since the exact values of the thermal conductivities of both layers are not accurately known.

The measured difference signals are converted into the near-field radiative heat transfer magnitude by using the power sensitivity value S_P. As the conductance of the cantilever is known, the temperature of the sphere can be found using Eq. (3.3). The near-field radiative conductance can be obtained by dividing the near-field radiative heat transfer by the temperature difference between the sphere and the substrate.

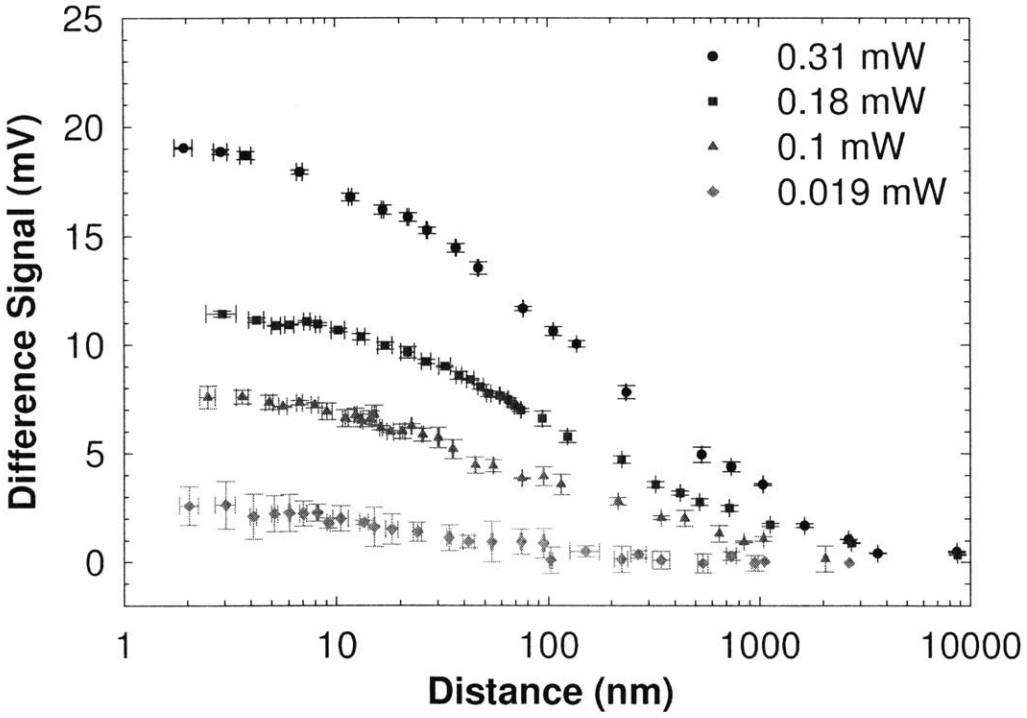

(a)

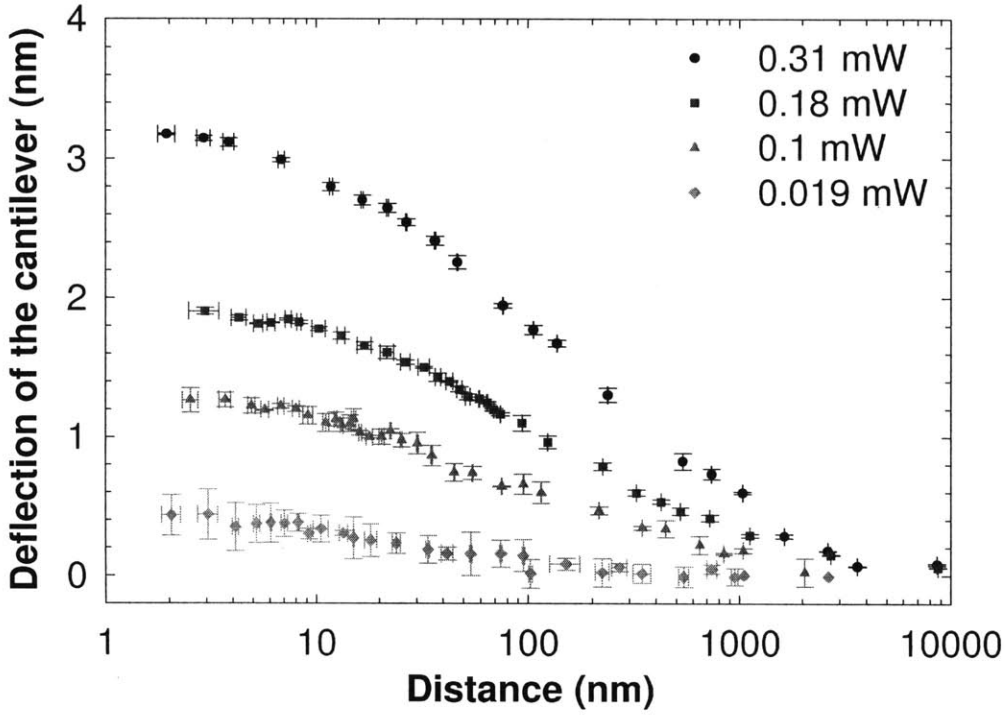

(b)

Figure 4.2 (a) Difference signals for four different laser powers. (b) The deflection of the cantilever for four different laser powers. The signal due to the force is obtained by taking measurements under very weak laser power (0.019 mW). Under very weak laser power, the temperature difference between the sphere and the substrate is expected to be very small.

Fig. 4.3 shows preliminary experimental results for near-field radiative conductance as a function of separation gap at three distinct temperature differences, ΔT = 13 K, 24 K, and 41 K, correspond to different laser powers. The theoretical conductance values are based on the Proximity Force Theorem and calculated with local dielectric constant. Theoretical analysis predicts that the near-field radiative conductance increases proportionally with the temperature difference between the sphere and the substrate. However, occasionally the near-field radiative conductance at ΔT = 13 K is higher than at ΔT = 41 K and 24 K, thus disagreeing with theory. The underlying reason is because our experimental setup is not sensitive enough to resolve radiative conductance at such small changes in temperature difference. Fig. 4.2 shows that the deflection signal is proportional to the temperature difference with the noise level being inversely

proportional to the temperature difference. Hence, a smaller temperature difference corresponds to a reduced signal-to-noise ratio. To overcome this problem, larger temperature differences need to be applied, something planned in future works.

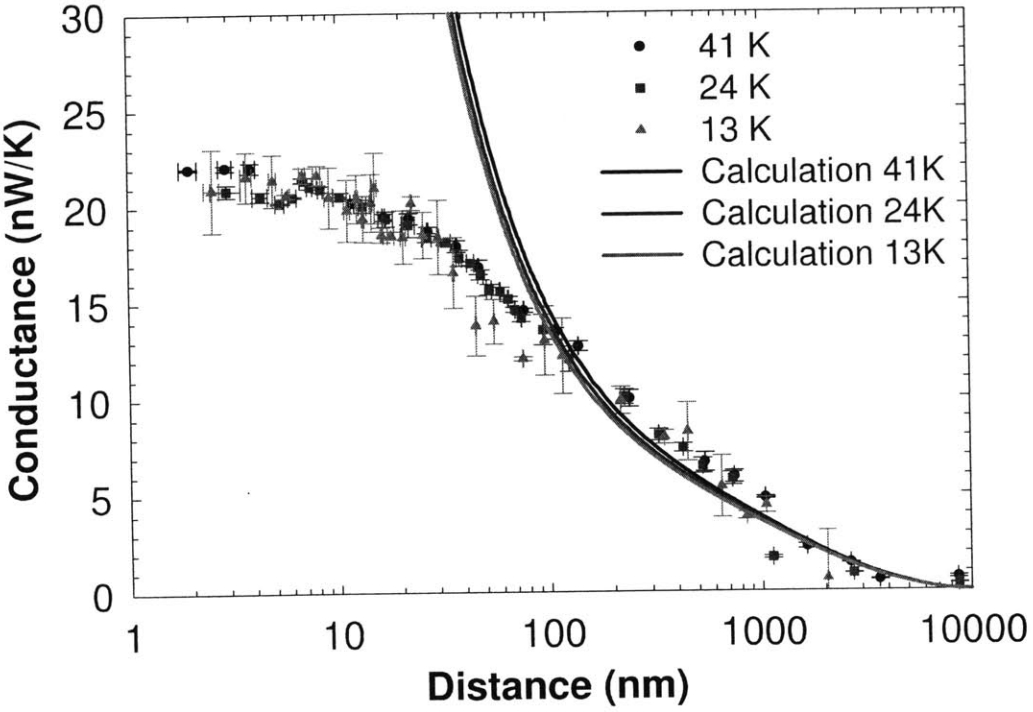

Figure 4.3 Preliminary experimental data for near-field radiative conductance between a silica sphere of 100μm diameter and a glass substrate at very small separation distance and for three temperature differences. The calculation is based on the Proximity Force Approximation.

The experimental results reasonably fit the theoretical calculation based on the proximity force approximation when the separation distances are larger than 100nm. This result agrees with the assertion by Shen *et al.* [30] that the use of the proximity force approximation gives a reasonable approximation. Below 100 nm, the experimental results start deviating from the theoretical analysis. Saturation in the near-field radiative conductance is observed below 30 nm. Since we do not know whether the saturation of the radiative heat transfer is due to only the spatial dispersion of dielectric constant, all other potential reasons that may cause saturation of the radiative heat transfer must be identified and removed.

4.2 Saturation of the Near-field Radiative Heat Transfer

Two effects other than the non-local effect of dielectric constant are considered to cause saturation, surface roughness of the microsphere and the repulsive force.

4.2.1 Surface Roughness

When the separation distance between the sphere and the plate is comparable or smaller than the surface roughness, the surface roughness cannot just be considered as roughness anymore. The surface roughness has become the dominating structure of the surface of the sphere. To include the surface roughness into the calculation we adapt the Proximity Force Approximation. We assume that each differential plate has surface roughness as illustrated in Fig. 4.4.

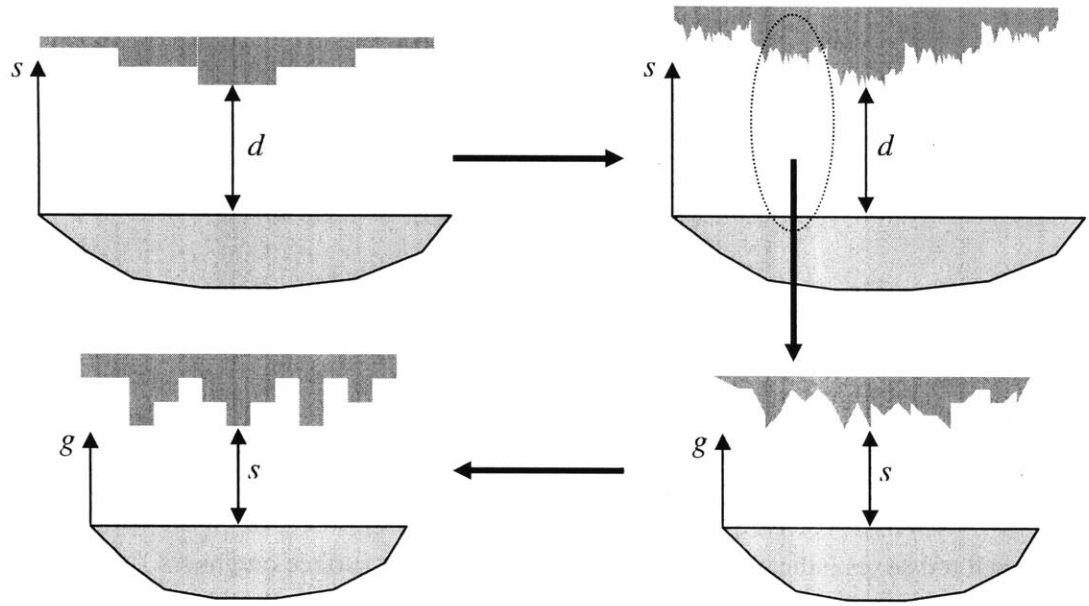

Figure 4.4 The modified Proximity Force Theorem. Each differential plate is a random structure surface.

Each differential plate with varying distance s from $s = d$ to $s = max\ depth$ is assumed to have an effective heat transfer coefficient $h(s)$ in the Proximity Force Approximation. The surface roughness is modeled on the differential plates with different separation distance g. The effective heat transfer coefficient thus reads:

$$h_{eff}(s) = \int_{s}^{\max depth} f(g)h(g)dg \tag{4.1}$$

$f(g)$ is a weighting function which is obtained from the distribution the surface roughness. The separation distance d is measured between the peak of the surface roughness and the substrate.

Fig. 4.5 shows an AFM image of the surface of the silica microsphere. The dark areas on the edges show the curvature of the sphere. To obtain the weighting function, we analyze small sample areas of ~100000 nm^2, illustrated by red boxes in the figure which are then averaged. Small sample areas are considered to avoid the influence of the sphere curvature in the surface roughness. Fig. 4.6 shows the average of the distribution of the surface roughness. This distribution is fitted with a Gaussian function to obtain a weighting function $f(g)$.

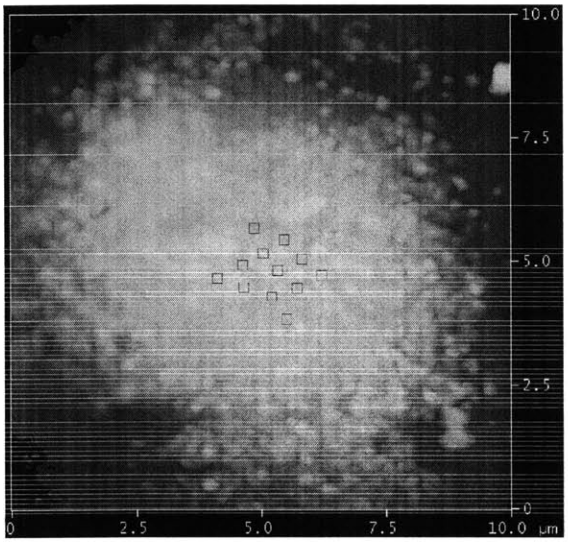

Figure 4.5 AFM image of the surface roughness of the silica microsphere. The scan size is 10x10 μm^2. Small red boxes indicate the sample areas to extract the surface roughness.

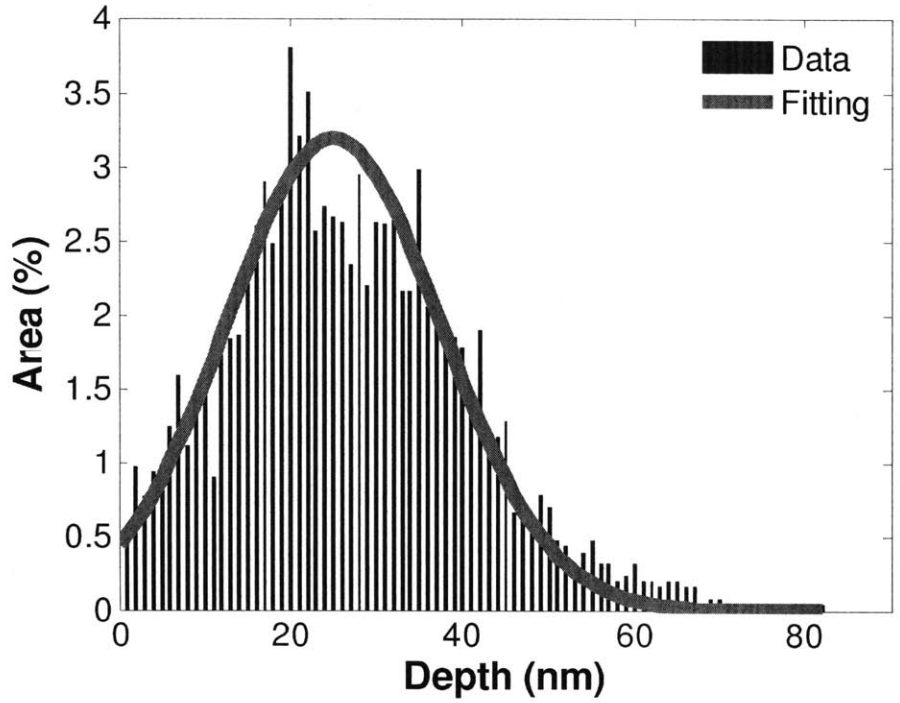

Figure 4.6 Histogram representing the distribution of the surface roughness averaged over 12 sample areas (as indicated by the red boxes in Figure 4.6). The red curve is a Gaussian fitting curve to the distribution.

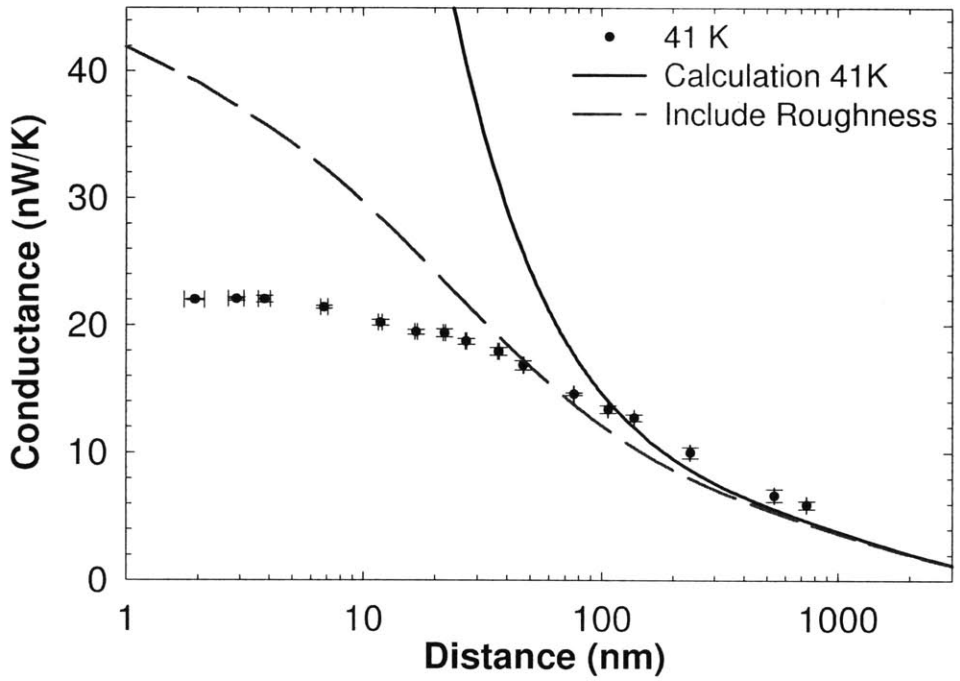

Figure 4.7 Modified Proximity Force Theorem results when including surface roughness.

Fig. 4.7 illustrates the calculated results by including the surface roughness described by Eq. (4.2). The result clearly demonstrates that the surface roughness can reduce the slope of the conductance of the near-field radiative heat transfer at small separations. The reduced slope is explained by Fig. 4.8. The separation distance is measured between the peaks of the surface roughness and the substrate. At small separation distances, even though these peaks theoretically contribute a very large radiative heat flux, they only occupy a small area. Hence, their contribution to the total heat transfer is limited. Meanwhile, a large fraction of the surface area of the sphere is at greater distance from the glass substrate. Even though these areas make up a smaller radiative heat flux, their cumulative contribution to the total radiative heat transfer is dominant. As a consequence it appears that the radiative heat transfer increases with a slower rate depending on the surface roughness profile.

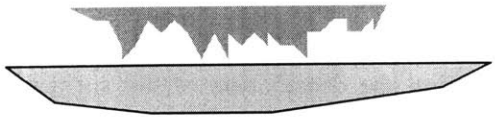

Figure 4.8 Schematic of the surface roughness. Notice that the separation distance is measured between the peaks of the surface roughness and the substrate.

At this point, we can not confirm whether the surface roughness is the primary cause of the saturation of the heat transfer observed in this experiment. Based on this simple analysis, we can only conclude that the surface roughness can reduce the slope of the near-field radiative transfer at small separations. To fully understand the significance of the surface roughness, a complete near-field heat transfer calculation between a rough sphere and a substrate needs to be performed.

4.2.2 Repulsive Forces

The force correction was done following the procedure explained in the previous section. The temperature difference between the sphere and the substrate at very weak laser power (0.019 mW) was measured to be 2.5 K. This temperature difference is not sufficiently small to measure the force between the sphere and the substrate. The heat

transfer is believed to still contribute to the deflection of the cantilever. Hence, we conclude that the force correction done in Section 4.1 is not very accurate.

Here, we propose a possibility that the saturation in the near-field radiative transfer is caused by repulsive forces. As explained in Section 3.2, due to the orientation of the cantilever relative to the substrate, it will bend in counter-clockwise direction when the separation distance between the sphere and the substrate becomes small. Consequently, the saturation of the near-field radiative heat transfer can also occur due to torque in clock wise direction of the cantilever

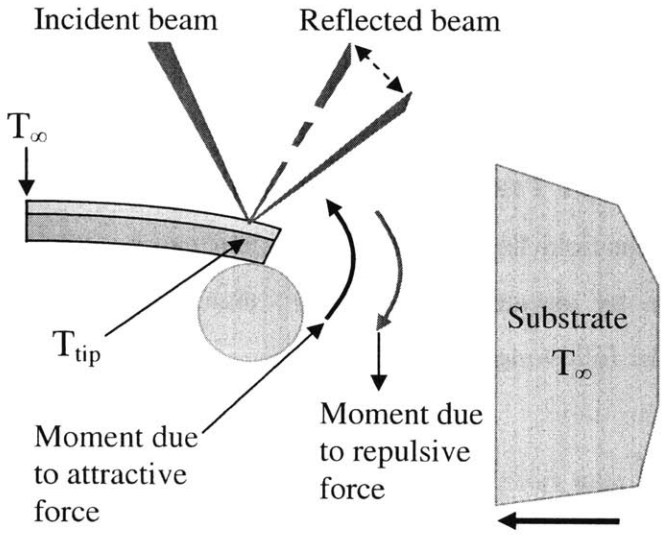

Figure 4.9 Schematic of the bending of the cantilever resulting from repulsive forces.

Electrostatic and Casimir forces are two possibilities for this condition to arise. There is a small possibility that this saturation is caused by Casimir forces. Repulsive Casimir force is very unlikely to happen in our case, since a special condition (shown in Fig. 4.10) needs to be satisfied in order for repulsive Casimir forces to occur. Therefore, we conclude that repulsive electrostatic forces might be the cause of the saturation.

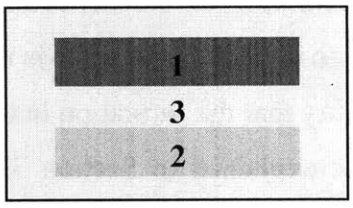

$\varepsilon_1(i\omega) > \varepsilon_3(i\omega) > \varepsilon_2(i\omega)$

Figure 4.10 Condition for repulsive Casimir forces [65].

To prove this possibility, the force measurement between the sphere and the substrate needs to be performed with a smaller temperature difference (<1K) to ensure that the heat transfer does not contribute to the measurement.

4.3 Near-Field Heat Transfer Coefficient

The equivalent near-field heat transfer coefficient can be extracted from the near-field conductance data by assuming an effective area, $A_{eff}(d)$. The effective area can be calculated from the following expression.

$$G(d) = A_{eff}(d)h(d) \tag{4.2}$$

where $G(d)$ is the near-field conductance calculated using the proximity force theorem and $h(d)$ is the calculated heat transfer coefficient. Since the effective area is obtained from the theoretical calculation, this method of obtaining the heat transfer coefficient works best when the experimental near-field conductance data match the theoretical calculation as shown in Fig. 4.3. Fig. 4.11 shows the equivalent near-field heat transfer coefficient data obtained through Eq. (4.2). The near-field heat transfer coefficients agree poorly with the theoretical calculation for separation distances below 100 nm, while there is reasonable agreement for separation distances between 100 nm and 4000 nm.

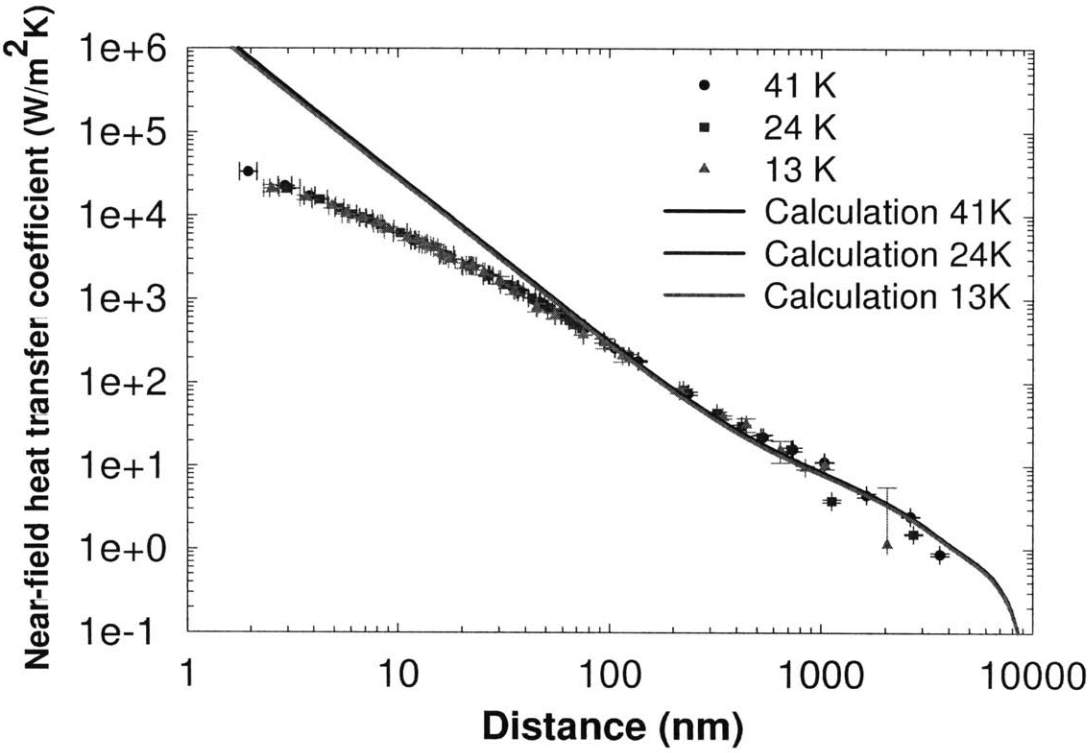
Near-field heat transfer coefficient (W/m^{2}K)
1e+6
1e+5
1e+4
1e+3
1e+2
1e+1
1e+0
1e-1
1
10
100
1000
10000
Distance (nm)
41 K
24 K
13 K
Calculation 41K
Calculation 24K
Calculation 13K

(a)

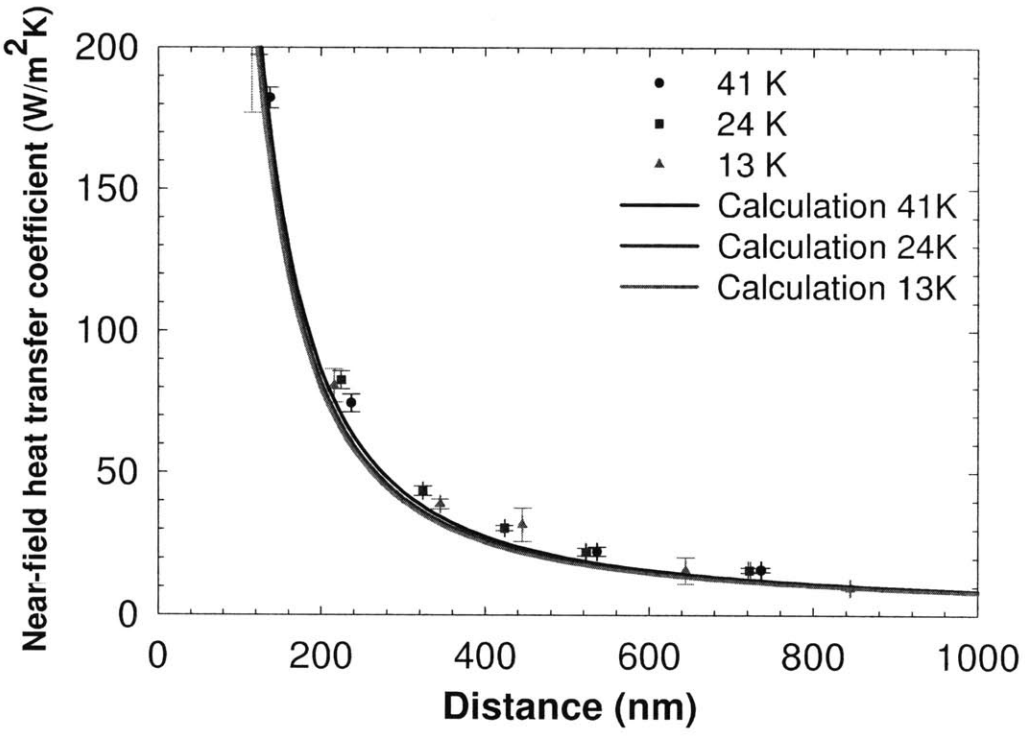
Near-field heat transfer coefficient (W/m^{2}K)
200
150
100
50
0
0
200
400
600
800
1000
Distance (nm)
41 K
24 K
13 K
Calculation 41K
Calculation 24K
Calculation 13K

(b)

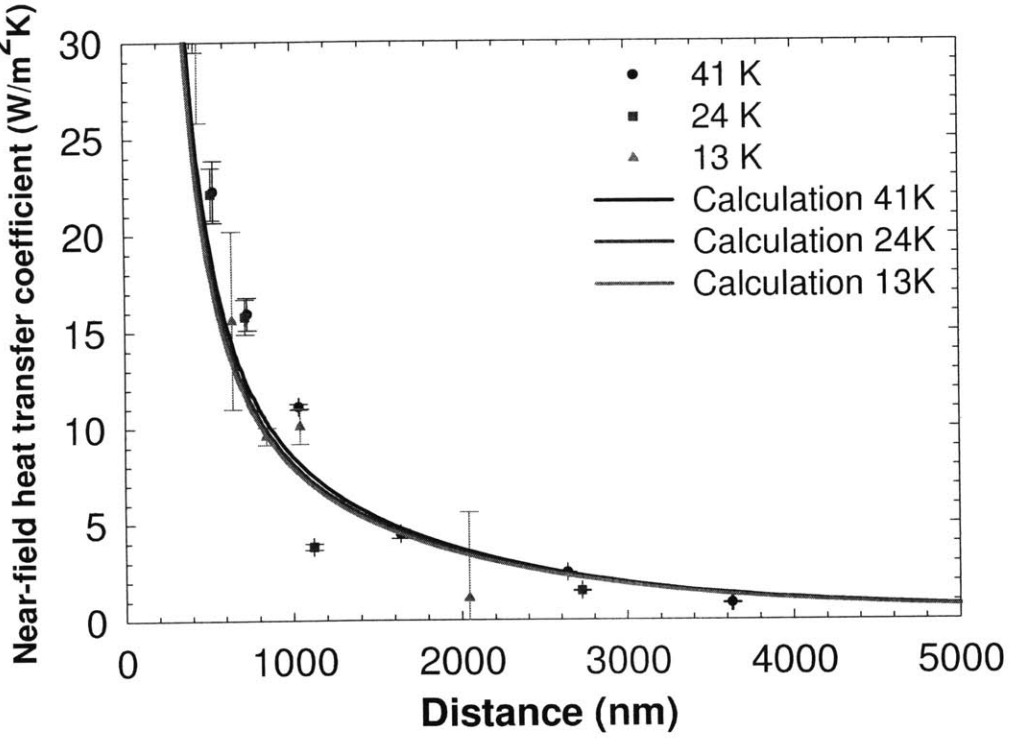

(c)

Figure 4.11 Equivalent sphere-plate near-field heat transfer coefficient normalized to the effective area $A_{eff}(d)$ obtained from Eq. (4.2). (a) log-log scale. (b) Separation distance between contact point and 1000 nm. (c) Separation distance between contact point and 5000 nm.

4.4 Summary

Measurement of the near-field radiative transfer between a silica microsphere of diameter 100 μm and a glass substrate are conducted. The heat transfer was measured for a plate-sphere separation distance as small as 2 nm. The experimental results fit the theoretical calculation reasonably when the separation distances are larger than 100 nm. Below 100 nm, the experimental results start deviating from the theoretical analysis. Saturation in the near-field radiative conductance is observed below 30 nm. Two effects other than the non-local effect of the dielectric constant are considered to cause saturation, surface roughness of the microsphere and the repulsive force. To include the surface roughness into the calculation we adapt the Proximity Force Approximation. Even though the result clearly demonstrates that the surface roughness can reduce the slope of the conductance of the near-field radiative heat transfer at small separations, it still does not explain the

saturation of the heat transfer. To fully understand the significance of the surface roughness, a complete near-field heat transfer calculation of between a rough sphere and a substrate needs to be performed. We then propose a possibility that the saturation in the near-field radiative transfer is caused by repulsive electrostatic forces. To prove this possibility, the force measurement with a smaller temperature difference (<1K) between the sphere and the substrate needs to be performed to ensure that the heat transfer does not contribute to the measurement. We also show the equivalent near-field heat transfer coefficient. The experimental data does not agree with the theoretical calculation for separation distances below 100 nm, while it agrees reasonably well for separation distances between 100 nm and 4000 nm following the agreement of the near-field conductance data.

Chapter 5

Summary and Future Directions

5.1 Summary

We have presented preliminary results of the near-field radiative heat transfer measurement between a silica microsphere and glass substrate for separation distances as small as 2 nm. The results deviate substantially from the theoretical predictions for a separation distance of 100 nm and start to saturate at a separation distance of 30 nm. The observed saturation seems to occur at too large a separation distance to be caused by the spatial dispersion of the dielectric constant. Two other effects are considered to cause saturation: surface roughness of the microsphere and the repulsive force. Surface roughness is included in the analytical analysis of the radiative heat transfer through an approximate model of the Proximity Force Theorem. Even though the result clearly demonstrates that the surface roughness can reduce the slope of the conductance of the near-field radiative heat transfer at small separations, it still does not explain the saturation of the heat transfer. To fully understand the significance of the surface roughness, a complete near-field heat transfer calculation of between a rough sphere and a substrate needs to be performed. We then propose a possibility that the saturation in the near-field radiative transfer is caused by a repulsive electrostatic force. To prove this possibility, the force measurement with smaller temperature difference (<1K) between the sphere and the substrate needs to be performed to ensure that the heat transfer does not contribute to the measurement.

The experimental results fit the theoretical calculation based on the proximity force approximation reasonably when the separation distances are larger than 100nm. This

result agrees with the assertion by Shen *et al.* [30] that the proximity force approximation gives a reasonable approximation. In contrast with Rosseau *et al.* [31], based on the preliminary results, we conclude that more measurements with better accuracy need to be done before we can claim the validity of the proximity force approximation.

5.2 Future Directions

Currently, surface roughness of the microsphere and potentially also the electrostatic force prevent us from obtaining a conclusive result. To reduce the surface roughness, we will continue to improve our heat and mechanical treatment of the microspheres to make them smoother. Further tests will be carried out to minimize the influence of the electrostatic force. On the theoretical side, a rigorous calculation which includes the surface roughness will be performed.

To study the effect of temperature on the near-field radiative heat transfer, more experiments at higher temperature differences needs to be carried out to overcome the problem of low signal-to-noise ratio. Fig. 5.1 shows the near-field radiative conductance as function of temperature difference.

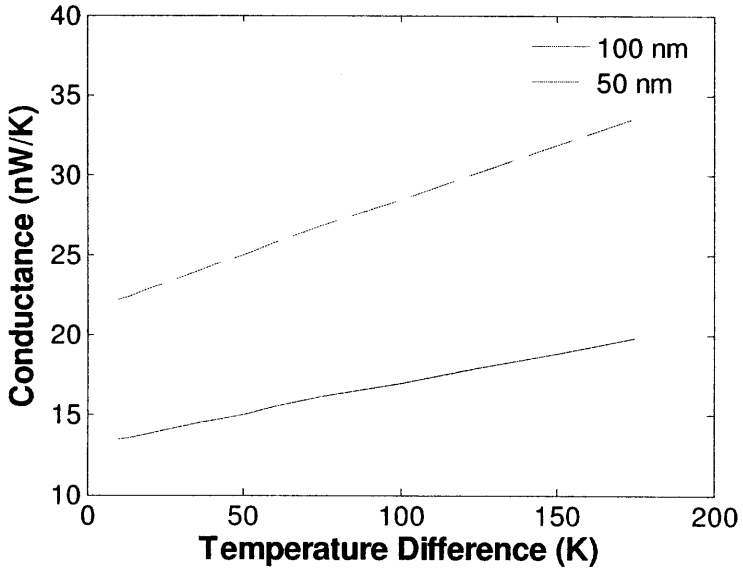

Figure 5.1 Near-field radiative conductance between a silica sphere of 100 μm diameter and a glass substrate as a function of temperature difference for two separation distances, 100 nm and 50 nm.

Bibliography

[1] M. Modest *Radiative Heat Transfer.* Academic Press, 2003.

[2] Planck, M. *The Theory of Heat Radiation* (Dover Publications, New York, 1991).

[3] S. M. Rytov. *Theory of Electric Fluctuations and Thermal Radiation.* Air Force Cambridge Research Center, Bedford, MA, 1959.

[4] Rytov, S. M., Kravtsov, Y. A., and Tatarski V. I., 1987, *Principles of Statistical Radiophysics*, Springer-Verlag, N. Y.

[5] E. G. Cravalho, C. L. Tien, and R. P. Caren. Effect of small spacings on radiative transfer between two dielectrics. *J. Heat Trans.*, 89(4):351–358, 1967.

[6] D. Polder and M. Van Hove. Theory of radiative heat transfer between closely spaced bodies. *Physical Review B*, 4(10):3303–3314, 1971.

[7] J. J. Loomis and H. J. Maris. Theory of Heat Transfer by Evanescent Electromagnetic Waves. *Physical Review B*, Vol. 50, pp. 18517-18524, 1994.

[8] A. Shchegrov, K. Joulain, R. Carminati, and J. –J. Greffet. Near-field Spectral Effects due to Electromagnetic Surface Excitations," *Physical Review Letter*, Vol 85, pp.1548-1551, 2000.

[9] C. J. Fu, and W. C. Tan. Near-field Radiative Heat Transfer between Two Plane Surfaces with One having a Dielectric Coating. *Journal of Quantitative Spectroscopy and Radiative Transfer*, Vol. 110, pp. 1027-1036, 2009.

[10] M. Francoeur, M. P. Menguc, and R. Vaillon. Near-field Radiative Heat Transfer Enhancement via Surface Phonon Polaritons Coupling in Thin Films. *Applied Physics Letters*, Vol. 93, p. 043109, 2008.

[11] P. Ben-Abdallah, K. Joulain, J. Drevellion, and G. Domingues. Near-Field Heat Transfer Mediated by Surface Wave Hybridization between Two Films. *Journal of Applied Physics*, Vol. 106, p. 044306, 2009.

[12] J. P. Mulet, K. Joulain, R. Carminati, and J. –J. Greffet. Nanoscale Radiative heat Transfer between A Small Particle and a Plane Surface. *Applied Physics Letters*, Vol. 78, pp. 2931-2933, 2001.

[13] A. Narayanaswamy, and G. Chen. Thermal Near-field Radiative Transfer between Two Spheres," *Physical Review B*, Vol. 77, p. 075125, 2008.

[14] C. J. Fu, and Z. M. Zhang. Nanoscale Radiation Heat Transfer for Silicon at Different Doping Levels. *International Journal of Heat and Mass Transfer*, Vol. 49, pp. 1703-1718, 2006.

[15] S. Basu, B. J. Lee, and Z. M. Zhang. Near-field Radiation Calculated with an Improved Dielectric Function Model for Doped Silicon. *Journal of Heat Transfer*, 2009.

[16] E. Rousseau, M. Laroche, and J. –J. Greffet. Radiative Heat Transfer at Nanoscale Mediated by Surface Plasmons for Highly Doped Silicon.

[17] K. Joulain, J. Drevillon, and P. Ben-Abdallah. Noncontact Heat Transfer between Two Metamaterials. *Physical Review B*, Vol 81, 165119, 2010.

[18] Z. M. Zhang and C. J. Fu. Unusual Photon Tunneling in The Presence of a Layer with a Negative Refractive Index. *Applied Physics Letters*, Vol 80, 2002.

[19] M. Laroche, R. Carminati, and J. –J, Greffet. Near-field Thermophotovoltaic Energy Conversion. *Journal of Applied Physics*, Vol. 100, p. 063704, 2006.

[20] K. Park, S. Basu, W. P. King, and Z. M. Zhang. Performance Analysis of Nearfield Thermophotovoltaic Devices Considering Absorption Distribution. *Journal of Quantitative Spectroscopy and Radiative Transfer*, Vol. 109, pp. 305-316, 2008.

[21] Z. W. Liu, Q. H. Wei, and X. Zhang. Surface Plasmon Interference Nanolithography. *Nano Letters*, Vol. 5, pp. 957-961, 2005

[22] L. Wang, S. M. Uppuluri, E. X. Jin, and X. F. Xu. Nanolithography Using High Transmission Nanoscale Bowtie Apertures. *Nano Letters*, Vol. 6, pp. 361-364, 2006

[23] Y. De Wilde, F. Formanek, R. Carminati, B. Gralak, P. A. Lemoine, K. Joulain, J. P. Mulet, Y. Chen, and J. –J. Greffet. Thermal Radiation Scanning Tunneling Microscopy. *Nature*, Vol. 444, pp. 740-743, 2006.

[24] G. A. Domoto, R. F. Boehm, and C. L. Tien. Experimental investigation of radiative transfer between metallic surfaces at cryogenic temperatures. *J. Heat Transfer* **92**, 412-417, 1970.

[25] C. M. Hargreaves. Anomalous radiative transfer between closely-spaced bodies. *Phys. Lett.* 30A, 491-492, 1969.

[26] J. B. Xu, K. Lauger, R. Moller, K. Dransfeld, and I. H. Wilson. Heat Transfer between Two Metallic Surfaces at Small Distances. *Journal of Applied Physics* Vol. 76, pp. 7209-7216, 1994.

[27] A. Kittel, W. Muller-Hirsch, J. Parisi, S. A. Biehs, D. Reddig, and M. Holthaus. Near-field Heat Transfer in a Scanning Thermal Microscope," *Physical Review*

Letters, Vol. 95, p. 224301, 2005.

[28] A. Narayanaswamy, S. Shen, and G. Chen. Near-field Radiative Heat Transfer between a Sphere and a Substrate," *Physical Review B*, Vol. 78, p.115303, 2008.

[29] L. Hu, A. Narayanaswamy, X. Y. Chen, and G. Chen. Near-field thermal radiation between two closely spaced glass plates exceeding Planck's blackbody radiation law. *Appl. Phys. Lett.* **92**, 133106, 2008.

[30] S. Shen, A. Narayanaswamy, and G. Chen. Surface phonon polaritons mediated energy transfer between nanoscale gaps. *Nano Lett.* **9**, 2909-2913, 2009.

[31] E. Rousseau, A. Siria, G. Jourdan, S. Volz, F. Comin, J. Chevrier, J. –J. Greffet. Radiative Heat Transfer at the Nanoscale. *Nature Photonics*, v. 3, pp. 514-517, 2009.

[32] J. B. Pendry. Radiative exchange of heat between nanostructures. *J. Phys.* : *Condens. Matter* **11**, 6621, 1999.

[33] S. Basu, and Z. M. Zhang. Maximum Energy Transfer in Near-field Thermal Radiation at Nanometer Distances," *Journal of Applied Physics* Vol. 105, 093535, 2009.

[34] X. J. Wang, S. Basu, and Z. M. Zhang. Parametric Optimization of Dielectric Functions for Maximizing Nanoscale Radiative Transfer. *Journal of Physics D: Applied Physics*, 42, 2009.

[35] P. Ben-Abdallah, and K. Joulain. Fundamental Limits for Noncontact Transfer between Two Bodies," *Physical Review B*, 82, 2010.

[36] J. L. Pan. Radiative Transfer Over Small Distances from a Heated Metals. *Optics Letter*, Vol 25, No 6, 2000.

[37] A. I. Volokitin and B. N. Persson. Radiative Heat Transfer between Nanostructures. *Physical Review B*, Vol. 63, p. 205404, 2001.

[38] A. I. Volokitin and B. N. Persson. Resonant Photon Tunneling Enhancement of the Radiative Heat Transfer. *Physical Review B*, Vol. 69, p. 045417, 2004.

[39] P. O. Chapuis, S. Volz, C. Henkel, K. Joulain, and J. –J. Greffet. Effects of Spatial Dispersion in Near-field Radiative Heat Transfer between Two Parallel Metallic Surfaces. *Physical Review B*, Vol. 77, p. 035431, 2008.

[40] K. Joulain. Near-field Heat Transfer: A Radiative Interpretation of Thermal Conduction," *Journal of Quantitative Spectroscopy and Radiative Transfer*, Vol.109, pp. 294-304, 2008.

[41] C. Henkel and K. Joulain. Electromagnetic Field Correlations Near a Surface with a Nonlocal Optical Response. *Applied Physics B*, Vol.84, pp. 61-68, 2006.

[42] B. E. Sernelius. Effects of Spatial Dispersion on Electromagnetic Surface Modes and on Modes Associated with a Gap between Two Half Spaces. *Physical Review B* 71, 235114, 2005.

[43] L. Tsang, J. A. Kong, and K. H. Ding, *Scattering of Electromagnetic Waves*,Wiley, New York, 2000.

[44] A. Narayanaswamy, and G. Chen. Direct computation of thermal emission from nanostructures. *Annu Rev Heat Transfer*, 14:169–95, 2005.

[45] G. Chen. *Nanoscale Energy Transport and Conversion*, Oxford, New York, 2005.

[46] H. B. Callen, and T. A. Welton. Irreversibility and generalized noise. *Phys. Rev.*, 83(1):34–40, 1951.

[47] L. D. Landau and E. M. Lifshitz. *Statistical Physics*. Addison-Wesley, 1969.

[48] J. Weber. Fluctuation dissipation theorem. *Phys. Rev.*, 101(6):1620–1626, 1956.

[49] Mulet J-P, Joulain K, Carminati R, Greffet J-J. Enhanced radiative heat transfer at nanometric distances. *Microscale Thermophys Eng* 6:209–22, 2002.

[50] M. Francoeur, and M. P. Menguc. Role of Fluctuational Electrodynamics in Near-Field Radiative Heat Transfer. *Journal of Quantitative Spectroscopy and Radiative Transfer*, Vol. 109, pp. 280-293, 2008.

[51] Raether, H. *Surface Plasmons on Smooth and Rough Surfaces and on Gratings,* Springer-Verlag, Berlin , 1988.

[52] S. Shen. *Probing Extraordinary Nanoscale Energy Transfer Using Bimaterial Microcantilevers. urface Plasmons on Smooth and Rough Surfaces and on Gratings*. PhD Thesis, MIT, Cambridge, 2010.

[53] E. Palik. *Handbook of Optical Constants of Solids,* Academic Press, 1985.

[54] L. D. Landau, E. M. Lifshitz, and L. P. Pitaevskii. *Electrodynamics of Continuous Media*. Butterworth-Heinenann, 1996.

[55] K. L. Kliewer, and R. Fuchs. Theory of Dynamical Properties of Dielectric Surfaces, *Advances in Chemical Physics*, Vol. 27, 1974.

[56] G. Ford, and W. Weber. Phys Rep. 113, 195, 1984.

[57] H. B. G. Casimir, *Proc. K. Ned. Akad. Wet.* 60, 793, 1948.

[58] E.M. Lifshitz. The Theory of Molecular Attractive Forces between Solids. *Sov. Phys. JETP*, Vol. 2, pp. 73, 1956.

[59] A. Narayanaswamy. *Investigation of Nanoscale Thermal Radiation: Theory and Experiments*, PhD Thesis, MIT, Cambridge, 2007.

[60] J. R. Barnes, R. J. Stephenson, C. N. Woodburn, S. J. O'Shea, M. E. Welland, T. Rayment, J. K. Gimzewski, and Ch. Gerber. A femtojoule calorimeter using micromechanical sensors. *Review of Scientific Instruments*, 65:3793–3798, 1994.

[61] S. Shen, A. Narayanaswamy, S. Goh, and G. Chen. Thermal conductance of bimaterial microcantilevers. *Appl. Phys. Lett.* 92, 63509, 2008.

[62] E. P. Popov. *Mechanics of materials*. Englewood Cliffs, N.J.: Prentice-Hall, 1976.

[63] D. Song. *Phonon Heat Conduction on Nano and Micro-Porous Thin Films*, PhD Thesis, University of California, Los Angeles, 2003.

[64] G. Langer, J. Hartmann, and M. Reichling. Thermal conductivity of thin metallic films measured by photothermal profile analysis. *Review of Scientific Instruments*, 68:1510, 1996.

[65] F. Capasso. *Attractive and Repulsive Casimir-Lifshitz Forces: Vacuum Fluctuations, Quantum Levitation and Future of Nanomachines*. SIF Meeting, Bologna, 2010.